Draft version 2019.12.12.128
Typeset using LaTeX **twocolumn** style in AASTeX62

Modeling Dust and Starlight in Galaxies Observed by *Spitzer* and *Herschel*: The KINGFISH Sample

G. Aniano,[1,2] B. T. Draine,[1] L. K. Hunt,[3] K. Sandstrom,[4] D. Calzetti,[5] R. C. Kennicutt,[6,7] D. A. Dale,[8] M. Galametz,[9] K. D. Gordon,[10] A. K. Leroy,[11] J.-D. T. Smith,[12] H. Roussel,[13] M. Sauvage,[9] F. Walter,[14] L. Armus,[15] A. D. Bolatto,[16] M. Boquien,[17] A. Crocker,[18] I. De Looze,[19,20] J. Donovan Meyer,[21] G. Helou,[15] J. Hinz,[6] B. D. Johnson,[22] J. Koda,[23] A. Miller,[8,24] E. Montiel,[25,26] E. J. Murphy,[27] M. Relaño,[28,29] H.-W. Rix,[14] E. Schinnerer,[14] R. Skibba,[4,30] M. G. Wolfire,[16] and C. W. Engelbracht[31]

[1] *Dept. of Astrophysical Sciences, Peyton Hall, Princeton University, Princeton NJ 08544, USA*
[2] *LinkedIn Corporation, 700 E Middlefield Rd., Mountain View, CA 94043*
[3] *INAF - Osservatorio Astrofisico di Arcetri, Largo E. Fermi 5, 50125 Firenze, Italy*
[4] *Center for Astrophysics and Space Sciences, University of California, 9500 Gilman Drive, San Diego CA 92093, USA*
[5] *Dept. of Astronomy, University of Massachusetts, Amherst MA 01003, USA*
[6] *Steward Observatory, University of Arizona, Tucson AZ 85721-0065, USA*
[7] *Dept. of Physics & Astronomy, Texas A&M University, College Station TX 77843-4242, USA*
[8] *Physics & Astronomy Dept., University of Wyoming, Laramie WY 82071, USA*
[9] *AIM, CEA, CNRS, Université Paris-Saclay, Université Paris Diderot, Université Paris Cité, F-91191 Gif-sur-Yvette, France*
[10] *Space Telescope Science Institute, 3700 San Martin Drive, Baltimore MD 21218, USA*
[11] *Ohio State University, Columbus, OH 43210, USA*
[12] *Dept. of Physics & Astronomy, University of Toledo, Toledo, OH 43606, USA*
[13] *Institut d'Astrophysique de Paris, Université Pierre et Marie Curie (UPMC), Sorbonne Université, CNRS, 75014 Paris, France*
[14] *Max-Planck-Institut fur Astronomie, Konigstuhl 17, D-69117 Heidelberg, Germany*
[15] *Spitzer Science Center, California Institute of Technology, MC 314-6, Pasadena CA 91125, USA*
[16] *Dept. of Astronomy, University of Maryland, College Park MD 20742, USA*
[17] *Centro de Astronomía (CITEVA), Universidad de Antofagasta, Avenida Angamos 601, Antofagasta, Chile*
[18] *Dept. of Physics, Reed College, Portland OR 97202, USA*
[19] *Sterrenkundig Observatorium, Ghent University, Krijgslaan 281 S9, B-9000 Gent, Belgium*
[20] *Department of Physics & Astronomy, University College London, Gower St., London WC1E6BT, UK*
[21] *National Radio Astronomy Observatory, Charlottesville VA 22903, USA*
[22] *Harvard-Smithsonian Center for Astrophysics, Cambridge MA 02138, USA*
[23] *Department of Physics and Astronomy, SUNY Stony Brook, Stony Brook NY 11794-3800, USA*
[24] *Dept. of Physics, Montana State University, Bozeman MT 59717, USA*
[25] *University of California, Davis, Davis CA 95616, USA*
[26] *SOFIA Science Center, NASA Ames Research Center, Moffett Field CA 94036, USA*
[27] *National Radio Astronomy Observatory, Charlottesville VA 22903 USA*
[28] *Dept. Física Teórica y del Cosmos, Universidad de Granada, Granada, Spain*
[29] *Instituto Universitario Carlos I de Física Teórica y Computacional, Universidad de Granada, 18071, Granada, Spain*
[30] *Freelance science journalist, San Diego CA, USA*
[31] *deceased*

ABSTRACT

Dust and starlight are modeled for the KINGFISH project galaxies. With data from 3.6μm to 500μm, models are strongly constrained. For each pixel in each galaxy we estimate (1) dust surface density; (2) $q_{\rm PAH}$, the dust mass fraction in PAHs; (3) distribution of starlight intensities heating the dust; (4) luminosity emitted by the dust; and (5) dust luminosity from regions with high starlight intensity. The models successfully reproduce both global and resolved spectral energy distributions. We provide well-resolved maps for the dust properties. As in previous studies, we find $q_{\rm PAH}$ to be an increasing function of metallicity, above a threshold $Z/Z_\odot \approx 0.15$. Dust masses are obtained by summing the dust mass over the map pixels; these "resolved" dust masses are consistent with the masses inferred from model fits to the global photometry. The global dust-to-gas ratios obtained from

Corresponding author: B. T. Draine
draine@astro.princeton.edu

this study correlate with galaxy metallicities. Systems with $Z/Z_\odot \gtrsim 0.5$ have most of their refractory elements locked up in dust, whereas when $Z/Z_\odot \lesssim 0.3$ most of these elements tend to remain in the gas phase. Within galaxies, we find that $q_{\rm PAH}$ is suppressed in regions with unusually warm dust with $\nu L_\nu(70\mu{\rm m}) \gtrsim 0.4 L_{\rm dust}$. With knowledge of one long-wavelength flux density ratio (e.g., f_{160}/f_{500}), the minimum starlight intensity heating the dust ($U_{\rm min}$) can be estimated to within ∼50%. For the adopted dust model, dust masses can be estimated to within ∼0.07 dex accuracy using the 500μm luminosity $\nu L_\nu(500)$ alone. There are additional systematic errors arising from the choice of dust model, but these are hard to estimate. These calibrated prescriptions may be useful for studies of high-redshift galaxies.

1. INTRODUCTION

Interstellar dust affects the appearance of galaxies by attenuating short-wavelength radiation from stars and ionized gas, and contributing IR, submm, mm, and microwave emission. Dust is also an important agent in the fluid dynamics, chemistry, heating, cooling, and even ionization balance in some interstellar regions, with a major role in the process of star formation. Despite the importance of dust, determination of the physical properties of interstellar dust grains has been a challenging task [for a review, see Draine (2003)]. Even the overall amount of dust present in other galaxies has often been very uncertain.

The "Key Insights on Nearby Galaxies: a Far-Infrared Survey with Herschel" (KINGFISH) (Kennicutt et al. 2011) project is an imaging and spectroscopic survey of 61 nearby (distance $D < 30$ Mpc) galaxies with the *Herschel Space Observatory*. The KINGFISH galaxy sample was chosen to cover a wide range of integrated properties and local interstellar medium (ISM) environments found in the nearby Universe. KINGFISH is a direct descendant of the "*Spitzer* Infrared Nearby Galaxies Survey" (SINGS) (Kennicutt et al. 2003) which produced complete *Spitzer* imaging with the Infrared Array Camera (IRAC) (Fazio et al. 2004) and the Multiband Imaging Photometer for Spitzer (MIPS) (Rieke et al. 2004) instruments on *Spitzer Space Telescope* (Werner et al. 2004). The new *Herschel* observations include a complete mapping of the galaxies with the Photodetector Array Camera and Spectrometer (PACS) (Poglitsch et al. 2010) and the Spectral and Photometric Imaging Receiver (SPIRE) (Griffin et al. 2010) instruments. The merged KINGFISH and SINGS data-set provides panchromatic mapping of the galaxies, across a wide range of local extragalactic ISM environments. In addition, we have KINGFISH and SINGS data for 9 additional galaxies that fell within the 61 KINGFISH target fields. The photometric maps cover wavelengths from 3.6μm to 500μm, allowing us to produce well-resolved maps of the dust in nearby galaxies.

Skibba et al. (2011) modeled the dust in the KINGFISH galaxy sample using "modified blackbody" models. In the present work we employ a physically-motivated dust model based on a mixture of amorphous silicate grains and carbonaceous grains, each with a distribution of grain sizes (Draine & Li 2007, hereafter DL07). The dust grains are heated by starlight, and the model allows for a distribution of intensities for the starlight heating the dust. With a small number of adjustable parameters, the DL07 model reproduces the observed spectral energy distribution (SED) of the dust emission for a variety of astrophysical systems, giving some confidence in the reliability of dust masses estimated using the model. The DL07 model has been found to be consistent with the 3.6μm–500μm emission from the dust in the star-forming galaxies NGC 628 and NGC 6946 (Aniano et al. 2012), the dust across M31 (Draine et al. 2014), the emission from annular rings in the KINGFISH galaxy sample (Hunt et al. 2015), and the overall dust SEDs from KINGFISH galaxies (Dale et al. 2017).

The present work is a sequel to the KINGFISH study of NGC 628 and NGC 6946 (Aniano et al. 2012, hereafter AD12). AD12 developed the image processing and dust modeling techniques employed here, using the spiral galaxies NGC 628 and NGC 6946 as examples. The present work takes into account a recent "recalibration" of the DL07 model made possible by *Planck* observations of diffuse Galactic emission (Planck Collaboration et al. 2016). We expand the spatially-resolved dust modeling to the full KINGFISH galaxy sample, producing maps of dust mass surface density, PAH fraction, and intensities of the starlight heating the dust. Dependences of dust/gas ratio and PAH abundance on galaxy metallicity are examined, and resolved trends within galaxies are studied. While the present results are undoubtedly model-dependent, comparison of different dust models is beyond the scope of the present work.

The paper is organized as follows. A brief overview of the KINGFISH sample is given in Section 2, and in Section 3 we discuss the data sources. Background subtraction and data processing are described in Section 4, and the dust model is summarized in Section 5, including the *Planck*-based dust mass "recalibration" (Section 5.2). Results are reported in Section 6 with a comparison of dust parameter estimates based on different dust modeling strategies given in Section 6.4; global trends with metallicity are described in Sections 6.5 and 6.6; and resolved trends of DL07 fitted parameters are discussed in Sect. 6.7. We summarize the main results in Section 7. Appendix A (on-line version) displays maps of selected dust parameters for each of the 62 galaxies where we have reliable dust detections, at both MIPS160 and SPIRE250 resolution. Appendix B describes the

Table 1. Subsamples

Sample	name	KF galaxies	Extra galaxies	Total
Full sample	KF70	61	9	70
Dust detected	KF62	53	9	62
H I detected	KF57	57	0	57
CO detected	—	35	0	35
CO upper limits	—	5	0	5

method used to obtain upper limits for the dust mass for the eight galaxies (5 dwarfs, 3 ellipticals) where we were unable to measure the dust mass reliably. The on-line data set with the KINGFISH data and dust models is described in Appendix C. In Appendix D we examine the robustness of the results as the PSF is reduced, precluding use of the lower-resolution cameras (e.g., MIPS160 and SPIRE500).

2. GALAXY SAMPLE

The observational program was designed to cover the 61 galaxies in the KINGFISH galaxy sample. Because we will also be discussing the 9 extra galaxies, and the statistical properties of various subsamples, we list these for clarity in Table 1. For each galaxy, we list in Table 2 the type, adopted distance, and major and minor optical radii (corresponding to ~25th mag arcsec^{-2} isophotes), all taken from Kennicutt et al. (2011, Table 1).

The galaxies IC 3583, NGC 586, NGC 1317, NGC 1481, NGC 1510, NGC 3187, NGC 4533, NGC 7335, and NGC 7337 were not part of the KINGFISH sample, but were observed because each happened to be in the field of view of a KINGFISH galaxy. For these galaxies, we have our standard imaging with PACS and SPIRE, as well as prior observations with IRAC and MIPS, so we are able to measure and model their SEDs with the same techniques as the KINGFISH galaxies. Information for these 9 "extra" galaxies is appended to many of the tables below.

2.1. *Metallicities*

Table 2 also lists the oxygen abundance $12 + \log_{10}(\mathrm{O/H})$ for the galaxies in our sample. These are "characteristic" abundances, which Moustakas et al. (2010) take to be the values at galactocentric radius $R = 0.4R_{25}$. For 6 of the KINGFISH galaxies (DDO154, IC 342, NGC 628, NGC 2146, NGC 3077, and NGC 5457) we use metallicities based on observations of weak lines (specifically, [NII]5726 and [OIII]4364) that allow "direct" determination of the electron temperature in the H I regions responsible for the line emission (van Zee et al. 1997; Pilyugin et al. 2007; Engelbracht et al. 2008; Storchi-Bergmann et al. 1994; Li et al. 2013; Croxall et al. 2016). For these galaxies we list the preferred weak line metallicities in the PP04N2 column.

For the remaining 55 KINGFISH galaxies, we consider two popular "strong line" estimators: the "PT"

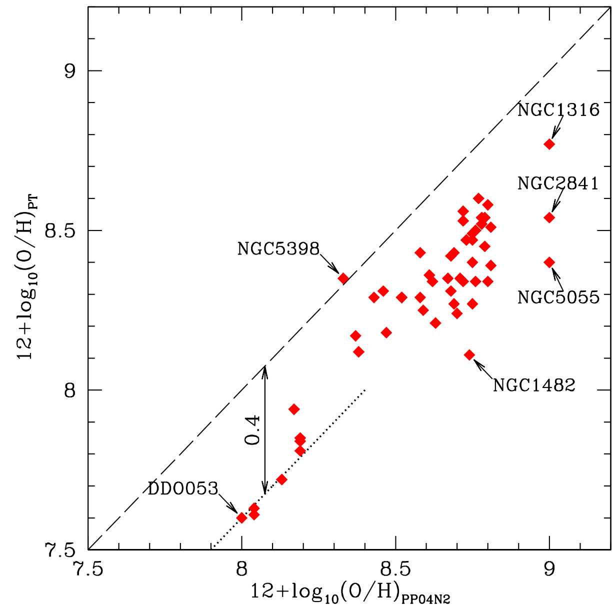

Figure 1. $12 + \log_{10}(\mathrm{O/H})$ for 55 KINGFISH galaxies using two different estimators (see text). The long-dashed line corresponds to identity between the two quantities. The PT estimate for O/H is systematically below the PP04N2 estimate (by ~0.4 dex at low O/H: dotted line), and there is considerable additional scatter between the two estimates.

Pilyugin & Thuan (2005) method, taken from Moustakas et al. (2010), and the "PP04N2" method based on [NII]/Hα (Pettini & Pagel 2004). Abundance measurements by Moustakas et al. (2010, "characteristic" values from their Table 8) with the "KK04" (Kobulnicky & Kewley 2004) calibration were converted to PP04N2 values, according to the parameters recommended by Kewley & Ellison (2008). This procedure is described in detail by Hunt et al. (2016) who use the same metallicities in their analysis; they preferred the PP04N2 calibration because it shows tighter scaling relations overall than other calibrations, and because its behavior in the mass-metallicity relation is quite similar to weak-line electron-temperature determinations (e.g., Andrews & Martini 2013).

For NGC 1316, NGC 2841, and NGC 5055 the original KK04 O/H values (~9.4) from Moustakas et al. (2010) exceeded the range of applicability for the transformations formulated by Kewley & Ellison (2008). Thus we have (somewhat arbitrarily) given these three galaxies a maximum metallicity of $12 + \log_{10}(\mathrm{O/H}) = 9.0$, consistent with what is advocated by Pilyugin et al. (2007). Ultimately, the metallicities for these three galaxies are uncertain, but toward the high end of the observed range.

Figure 1 compares the PT and PP04N2 metallicity estimates for the 55 KINGFISH galaxies where "direct" method estimates are unavailable. Note that the PT and

Table 2. The 61 KINGFISH galaxies + 9 extra galaxies

Galaxy	Type	$12+\log_{10}$(O/H) PT[a]	PP04N2[b]	D (Mpc)	optical $R_{\rm maj}$ (kpc)	$R_{\rm min}$ (kpc)	Ω (arcmin^2)	M160 mask $\Sigma_{Ld,\rm min}$ ($L_\odot$ pc^{-2})	Ω (arcmin^2)	S250 mask Ω (arcmin^2)
DDO053	Im	7.60 ± 0.11	8.00[c]	3.61	0.81	0.70	1.61	—	—	—
DDO154	IBm	7.54 ± 0.09	7.67[c]	4.30	1.89	1.36	5.15	—	—	—
DDO165	Im	7.63 ± 0.08	8.04[c]	4.57	2.30	1.22	4.98	—	—	—
Hol1	IABm	7.61 ± 0.11	8.04[c]	3.90	2.06	2.06	10.4	—	—	—
Hol2	Im	7.72 ± 0.14	8.13	3.05	3.52	2.78	39.0	0.72	25.2	23.0
IC342	SABcd	8.70 ± 0.20 [d]	8.85[e]	3.28	10.5	9.18	332.	3.47	417.	398.
IC2574	SABm	7.85 ± 0.14	8.19	3.79	7.27	2.72	51.1	0.66	54.5	52.7
M81dwB	Im	7.84 ± 0.13	8.19[c]	3.60	0.46	0.30	0.40	—	—	—
NGC0337	SBd	8.18 ± 0.07	8.47	19.30	8.08	4.98	4.01	3.55	11.1	6.77
NGC0584	E4	8.43 ± 0.20	8.69[c]	20.80	12.6	6.67	7.20	—	—	—
NGC0628	SAc	8.35 ± 0.01	8.64[f]	7.20	11.0	10.0	78.8	1.70	76.1	70.3
NGC0855	E	8.29 ± 0.10	8.43[c]	9.73	2.83	2.79	3.09	—	—	—
NGC0925	SABd	8.25 ± 0.01	8.59	9.12	13.9	7.57	47.0	1.48	46.3	44.8
NGC1097	SBb	8.47 ± 0.02	8.75	14.20	19.3	12.9	45.8	2.19	66.3	55.7
NGC1266	SB0	8.29 ± 0.20	8.52	30.60	6.85	6.75	1.83	2.63	9.09	8.37
NGC1291	SB0/a	8.52 ± 0.20	8.78	10.40	14.8	14.8	75.1	0.65	123.	119.
NGC1316	SAB0	8.77 ± 0.20	9.00[g]	21.00	12.2	8.49	8.73	1.02	17.5	14.2
NGC1377	S0	8.29 ± 0.20	8.52	24.60	6.37	6.37	2.49	2.57	7.20	8.46
NGC1404	E1	8.54 ± 0.20	8.78[c]	20.20	9.75	8.69	7.71	—	—	—
NGC1482	SA0	8.11 ± 0.13	8.74	22.60	8.09	4.40	2.59	2.19	24.4	13.0
NGC1512	SBab	8.56 ± 0.12	8.72	11.60	15.0	9.27	38.5	0.89	34.4	15.4
NGC2146	Sbab	8.68 ± 0.10 [e]	8.68[e]	17.20	16.8	7.35	15.5	4.8	39.2	18.5
NGC2798	SBa	8.34 ± 0.08	8.72	25.80	9.61	9.61	5.15	2.63	13.0	10.2
NGC2841	SAb	8.54 ± 0.03	9.00[g]	14.10	16.7	6.77	21.1	0.66	60.9	55.1
NGC2915	I0	7.94 ± 0.13	8.17	3.78	1.04	0.51	1.37	0.58	5.58	5.51
NGC2976	SAc	8.36 ± 0.06	8.61	3.55	3.04	1.28	11.5	2.57	25.6	21.3
NGC3049	SBab	8.53 ± 0.01	8.72	19.20	6.09	3.99	2.45	1.48	7.92	7.99
NGC3077	I0pec	—	8.64[h]	3.83	3.34	3.29	27.8	2.14	39.2	32.6
NGC3184	SABcd	8.51 ± 0.01	8.81	11.70	12.6	11.8	40.4	0.85	64.0	60.5
NGC3190	SAap	8.49 ± 0.20	8.75	19.30	12.2	3.78	4.61	1.17	12.3	11.2
NGC3198	SBc	8.34 ± 0.02	8.76	14.10	17.5	5.98	19.5	1.23	36.9	30.0
NGC3265	E	8.27 ± 0.14	8.69	19.60	3.65	2.80	0.99	2.04	6.39	6.10
NGC3351	SBb	8.60 ± 0.01	8.77	9.33	10.1	6.74	28.9	1.35	49.1	43.3
NGC3521	SABbc	8.39 ± 0.02	8.81	11.20	17.9	7.83	41.4	2.19	91.4	76.6
NGC3621	SAd	8.27 ± 0.02	8.75	6.55	11.7	6.55	66.4	1.07	103.	85.7
NGC3627	SABb	8.34 ± 0.24	8.62	9.38	12.4	5.26	27.6	2.00	87.2	54.9
NGC3773	SA0	8.43 ± 0.03	8.58	12.40	2.13	1.80	0.93	1.86	5.85	5.81
NGC3938	SAc	8.42 ± 0.20	8.68	17.90	14.0	12.8	20.8	1.15	39.4	34.5
NGC4236	SBdm	8.17 ± 0.20	8.37	4.45	10.4	2.85	55.4	0.71	64.7	63.2
NGC4254	SAc	8.45 ± 0.01	8.79	14.40	11.3	9.76	19.7	2.40	45.9	33.2
NGC4321	SABbc	8.50 ± 0.03	8.76	14.30	15.4	13.1	36.7	1.66	60.6	40.4
NGC4536	SABbc	8.21 ± 0.08	8.63	14.50	16.0	6.25	17.6	2.09	37.0	25.2
NGC4559	SABcd	8.29 ± 0.01	8.58	6.98	10.9	4.08	33.8	1.17	43.2	40.3
NGC4569	SABab	8.58 ± 0.20	8.80	9.86	11.5	4.85	21.2	1.95	18.3	17.2
NGC4579	SABb	8.54 ± 0.20	8.79	16.40	14.0	11.1	21.4	2.24	22.4	18.0
NGC4594	SAa	8.54 ± 0.20	8.79	9.08	11.5	2.98	15.5	1.55	31.1	27.8
NGC4625	SABmp	8.35 ± 0.17	8.67	9.30	2.95	2.55	3.23	1.58	7.47	6.47
NGC4631	SBd	8.12 ± 0.11	8.38	7.62	17.2	0.30	3.28	3.16	83.4	43.3
NGC4725	SABab	8.35 ± 0.13	8.71	11.90	18.6	12.9	62.7	1.15	64.1	55.0
NGC4736	SAab	8.31 ± 0.03	8.68	4.66	7.60	6.15	80.0	1.38	124.	120.
NGC4826	SAab	8.54 ± 0.10	8.78	5.27	6.13	4.70	38.5	2.88	37.3	17.3
NGC5055	SAbc	8.40 ± 0.03	9.00[g]	7.94	14.6	8.14	69.7	2.75	87.6	67.6
NGC5398	SBdm	8.35 ± 0.05	8.33	7.66	3.14	1.85	3.67	1.62	7.29	5.72
NGC5408	IBm	7.81 ± 0.09	8.19	4.80	1.13	0.53	0.97	2.95	6.66	5.42
NGC5457	SABcd	8.46 ± 0.10 [h]	8.38[i]	6.70	17.1	16.9	238.	0.74	398.	385.

a From Moustakas et al. (2010) except as noted
b Derived from KK metallicities from Moustakas et al. (2010) except as noted
c van Zee et al. (1997)
d Pilyugin et al. (2006)
e Engelbracht et al. (2008)
f Berg et al. (2015)
g see text
h Storchi-Bergmann et al. (1994)
i Li et al. (2013)

Table 2. continued.

Galaxy	Type	$12 + \log_{10}(\mathrm{O/H})$ PT	$12 + \log_{10}(\mathrm{O/H})$ PP04N2[a]	D (Mpc)	optical R_{maj} (kpc)	optical R_{min} (kpc)	optical Ω (arcmin^2)	M160 mask $\Sigma_{Ld,\mathrm{min}}$ ($L_\odot$ pc^{-2})	M160 mask Ω (arcmin^2)	S250 mask Ω (arcmin^2)
NGC5474	SAcd	8.31 ± 0.22	8.46	6.80	4.73	4.21	16.0	1.10	21.1	17.9
NGC5713	SABbc	8.24 ± 0.06	8.70	21.40	8.59	7.65	5.33	1.51	35.6	14.3
NGC5866	S0	8.47 ± 0.20	8.73	15.30	10.4	3.90	6.44	1.91	8.64	8.77
NGC6946	SABcd	8.400 ± 0.030	8.75	6.80	11.4	9.63	87.8	7.08	102.	100.
NGC7331	SAb	8.340 ± 0.020	8.80	14.50	22.1	6.83	26.7	3.02	47.1	32.3
NGC7793	SAd	8.310 ± 0.020	8.64	3.91	5.31	3.55	45.8	1.35	76.2	58.9
EIC3583	IBm	—	—	14.20	5.16	2.96	2.82	1.32	6.57	5.96
ENGC0586	SAa	—	—	20.80	5.63	1.92	0.93	0.78	5.31	4.93
ENGC1317	SABa	—	—	21.00	11.9	11.6	11.6	1.05	10.8	10.7
ENGC1481	SA0	—	—	22.60	3.68	2.90	0.78	0.98	5.40	2.00
ENGC1510	SA0	—	8.38[b]	11.60	2.80	2.15	1.66	0.95	7.74	1.76
ENGC3187	SBc	—	—	19.30	7.19	2.69	1.93	1.74	7.92	5.53
ENGC4533	SAd	—	—	14.50	5.48	0.38	0.37	1.12	6.12	3.83
ENGC7335	SAO	—	—	83.40	27.9	26.9	4.01	3.16	2.61	2.60
ENGC7337	SBb	—	—	87.20	25.1	21.7	2.67	2.00	2.16	1.98

a Derived from KK metallicities from Moustakas et al. (2010) except as noted *b* Marble et al. (2010)

PP04N2 metallicities differ by as much as 0.5 dex (e.g., DDO154, type IBm) or even 0.63 dex (e.g., NGC1482, type SA0). It is evident that the metallicity estimates have significant uncertainties, and that there are systematic differences between the two methods (see also Kewley & Ellison 2008). Below we will argue, by comparing PAH abundances estimated from infrared observations with these two metallicity estimates, that the PP04N2 estimate appears to be more reliable, at least for the galaxies in the KINGFISH sample.

3. OBSERVATIONS AND DATA REDUCTION

3.1. *Infrared, Far-Infrared, and Submm*

Most of the galaxies in the KINGFISH sample are part of the SINGS galaxy sample and were imaged by *Spitzer Space Telescope* as part of the SINGS observing program (Kennicutt et al. 2003). IRAC and MIPS imaging obtained by other *Spitzer Space Telescope* observing programs was available for the remaining KINGFISH galaxies.

The KINGFISH project imaged the galaxies with the *Herschel Space Observatory* (Pilbratt et al. 2010), following the observing strategy described by Kennicutt et al. (2011), using the 70, 100, and 160μm PACS filters, and the 250, 350, and 500μm SPIRE filters. The maps were designed to cover a region out to $\gtrsim 1.5$ times the optical radius R_{25}, with good signal to noise (S/N) and redundancy.

Following AD12, we will use "camera" to identify each optical configuration of the observing instruments, i.e., each different channel or filter arrangement of the instruments will be referred to as a different "camera". With this nomenclature, each "camera" has a characteristic spectral response and point-spread function (PSF). We will refer to the IRAC, MIPS, PACS, and SPIRE cameras using their nominal wavelengths in microns: IRAC3.6, IRAC4.5, IRAC5.8, IRAC8.0, MIPS24, MIPS70, MIPS160, PACS70, PACS100, PACS160, SPIRE250, SPIRE350, and SPIRE500.

IRAC imaged the galaxies in four bands, centered at 3.6μm, 4.5μm, 5.8μm, and 8.0μm, as described by Kennicutt et al. (2003). The images were processed by the SINGS Fifth Data Delivery pipeline.[1] The IRAC images are calibrated for point sources. Photometry of extended sources requires so-called "aperture corrections". We multiply the intensities in each pixel by the asymptotic (infinite radii) value of the aperture correction (i.e., the aperture correction corresponding to an infinite radius aperture). We use the factors 0.91, 0.94, 0.66 and 0.74 for the 3.6μm, 4.5μm, 5.8μm, and 8.0μm bands, respectively, as described in the IRAC Instrument Handbook (V2.0.1)[2].

Imaging with MIPS at 24, 70, and 160μm was carried out following the observing strategy described in Kennicutt et al. (2003). The data were reduced using the LVL (Local Volume Legacy) project pipeline.[3]. A correction for nonlinearities in the MIPS70 camera was applied, as described by Dale et al. (2009) and Gordon et al. (2011).

The galaxies were observed with the PACS and SPIRE instruments on *Herschel*, using the "Scan Map" observing mode. Both PACS and SPIRE images were first reduced to "level 1" (flux-calibrated brightness time series, with attached sky coordinates) using HIPE v11.1.0 (Ott 2010), and maps ("level 2") were created using the Scanamorphos data reduction pipeline (Roussel 2013), v24.0. This reduction strategy used the latest available PACS and SPIRE calibrations (as of 2014 July), and was designed to preserve the low surface brightness diffuse emission.

The assumed beam sizes are 465.4, 822.6, and 1769 arcsec^2 for SPIRE250, SPIRE350, and SPIRE500, respectively. Additionally, we excluded discrepant bolometers from the map and adjusted the pointing to match the MIPS24 map.

3.2. *H I Observations*

To measure the H I gas mass we use H I 21 cm line observations made with the NSF's NRAO[4] Karl G. Jansky Very Large Array (VLA).

For 23 of our galaxies we have data from The H I Nearby Galaxies Survey (THINGS Walter et al. 2008) and for four galaxies we use data from the LittleTHINGS survey (Hunter et al. 2012). For 10 galaxies without THINGS or LittleTHINGS observations, we obtained VLA 21-cm maps in programs AL731 and AL735, in some cases also incorporating archival VLA observations. For 8 targets, we reduced and incorporated VLA archival observations of the 21 cm line. For one galaxy, NGC 4559, we use archival WSRT observations. These observations are described in Leroy et al. (2013). For each galaxy, the source of the H I map is listed in Table 3. The dominant uncertainty on the measured H I masses comes from the calibration uncertainties of $\sim 10\%$.

For NGC 1266 Alatalo et al. (2011) estimated $M(\mathrm{H\,I}) = 9.5 \times 10^6 M_\odot$ based on 21 cm absorption of the radio continuum from the nucleus (for an assumed $T_{\rm spin} = 100\,\mathrm{K}$). However, we estimate that H I 21cm line emission from as much as $\sim 2 \times 10^9 M_\odot$ of H I could have gone un-

[1] Details can be found in the data release documentation: https://irsa.ipac.caltech.edu/data/SPITZER/SINGS/doc/sings_fifth_delivery_v2.pdf

[2] http://irsa.ipac.caltech.edu/data/SPITZER/docs/irac/iracinstrumenthandbook/IRAC_Instrument_Handbook.pdf

[3] Details can be found in the data release documentation: https://irsa.ipac.caltech.edu/data/SPITZER/LVL/LVL_DR5_v5.pdf

[4] The National Radio Astronomy Observatory is a facility of the National Science Foundation operated under cooperative agreement by Associated Universities, Inc.

detected because of the strong continuum (0.1 Jy at 1.4GHz), hence the H I mass must be considered highly uncertain.

Thus we have H I data for 57 of the 61 KINGFISH galaxies. H I 21 cm observations were not available for NGC 1316 (SAB0), NGC 1377 (S0), NGC 1404 (E1), NGC 5866 (S0), nor for the nine extra galaxies.

3.3. *CO Observations*

To estimate H_2 masses, we use observations of CO line emission together with an assumed ratio of H_2 mass to CO luminosity. The adopted CO-to-H_2 "conversion factors" are discussed in §4.5.

For 38 KINGFISH galaxies we use ^{12}CO $J = 2-1$ maps from the the HERA CO Line Emission Survey (HERACLES) (Leroy et al. 2009, 2013).

For NGC 4826, we use ^{12}CO $J=1$–0 mapping from the Nobeyama Radio Observatory (Koda et al. in prep). We propagate uncertainties on the CO integrated intensities from the spectra through the gridding and masking of the cube as described in Leroy et al. (2013).

For NGC 1266 we use $M(H_2) = 1.6 \times 10^9 M_\odot$ from Alatalo et al. (2011). We arbitrarily adopt a ±50% uncertainty. For NGC 3190 we use CO line fluxes from Martinez-Badenes et al. (2012).

Thus we have CO data for 41 of the 61 galaxies in the KINGFISH sample. CO observations are not available for any of the nine extra galaxies.

4. IMAGE ANALYSIS

4.1. *Background Subtraction*

All camera images are first rotated to RA/Dec coordinates, and then trimmed to a common sky region. For each image we estimate the best-fit "tilted plane" background (consisting of instrumental background, Galactic foreground emission, and cosmic infrared background emission) using an iterative procedure described in AD12. The procedure uses multiple cameras to identify regions in the image where only background emission is present. Regions where excess emission is detected at more than one wavelength are not used for background estimation.

4.2. *Convolution to Common Resolution*

After background subtraction, the images are convolved to a common point spread function (PSF), and resampled on a common final-map grid, with pixel sizes for each final-map PSF as given in Table 4. Finally, the dispersion in intensities of the background pixels (which includes noise coming from unresolved undetected background sources) is used to estimate the pixel flux uncertainties. By comparing the MIPS and PACS images, we can also estimate a calibration uncertainty. The procedures used are fully described in AD12.

As discussed in AD12, multiwavelength observations must be degraded to a common PSF before dust mod-

Table 3. H I & CO Observation Summary

Galaxy	H I Source	CO Source
DDO 053	LittleTHINGS	...
DDO 154	THINGS	HERACLES
DDO 165	LittleTHINGS	...
Holmberg I	THINGS	HERACLES
Holmberg II	THINGS	HERACLES
IC 342	Hyperleda	...
IC 2574	THINGS	HERACLES
M81 dwB	THINGS	HERACLES
NGC 0337	Archival	HERACLES
NGC 0584	Hyperleda	...
NGC 0628	THINGS	HERACLES
NGC 0855	Hyperleda	...
NGC 0925	THINGS	HERACLES
NGC 1097	Hyperleda	...
NGC 1266	ABY11	ABY11
NGC 1291	Hyperleda	...
NGC 1482	Hyperleda	...
NGC 1512	Hyperleda	...
NGC 2146	AL735	HERACLES
NGC 2798	AL735	HERACLES
NGC 2841	THINGS	HERACLES
NGC 2915	Hyperleda	...
NGC 2976	THINGS	HERACLES
NGC 3049	AL735	HERACLES
NGC 3077	THINGS	HERACLES
NGC 3184	THINGS	HERACLES
NGC 3190	AL735	MBLE12
NGC 3198	THINGS	HERACLES
NGC 3265	Hyperleda	...
NGC 3351	THINGS	HERACLES
NGC 3521	THINGS	HERACLES
NGC 3621	THINGS	...
NGC 3627	THINGS	HERACLES
NGC 3773	Hyperleda	...
NGC 3938	Archival, AL731	HERACLES
NGC 4236	AL731, AL735	HERACLES
NGC 4254	Archival, AL731	HERACLES
NGC 4321	Archival	HERACLES
NGC 4536	Archival, AL731, AL735	HERACLES
NGC 4559	Archival(WSRT)	HERACLES
NGC 4569	Archival	HERACLES
NGC 4579	Archival	HERACLES
NGC 4594	Archival, AL735	HERACLES
NGC 4625	Archival	HERACLES
NGC 4631	Archival	HERACLES
NGC 4725	AL735	HERACLES
NGC 4736	THINGS	HERACLES
NGC 4826	THINGS	CANON
NGC 5055	THINGS	HERACLES
NGC 5398	Hyperleda	...
NGC 5408	Hyperleda	...
NGC 5457	THINGS	HERACLES
NGC 5474	Archival	HERACLES
NGC 5713	Archival	HERACLES
NGC 6946	THINGS	HERACLES
NGC 7331	THINGS	HERACLES
NGC 7793	THINGS	...

THINGS = Walter et al. (2008)
HERACLES = Leroy et al. (2009, 2013)
ABY11 = Alatalo et al. (2011)
LittleTHINGS = Hunter et al. (2012)
MBLE12 = Martinez-Badenes et al. (2012)
Hyperleda = Makarov et al. (2014)
CANON = Donovan Meyer et al. (2013)

Table 4. Image Resolutions

Camera	FWHM[a] ($''$)	50% power[a] diameter ($''$)	Final grid pixel[b] ($''$)	Compatible cameras[c]
IRAC3.6	1.90	2.38	—	not used as a final-map PSF
IRAC4.5	1.81	2.48	—	not used as a final-map PSF
IRAC6	2.11	3.94	—	not used as a final-map PSF
IRAC8	2.82	4.42	—	not used as a final-map PSF
PACS70	5.67	8.46	—	not used as a final-map PSF
MIPS24	6.43	9.86	—	not used as a final-map PSF
PACS100	7.04	9.74	—	not used as a final-map PSF
PACS160	11.2	15.3	5.0	IRAC; MIPS24; PACS
SPIRE250 (S250)	18.2	20.4	6.0	IRAC; MIPS24; PACS; SPIRE250
MIPS70	18.7	28.8	10.0	IRAC; MIPS24,70; PACS; SPIRE250
SPIRE350	24.9	26.8	10.0	IRAC; MIPS24,70; PACS; SPIRE250,350
SPIRE500	36.1	39.0	15.0	IRAC; MIPS24,70; PACS; SPIRE
MIPS160 (M160)	38.8	58.0	18.0	IRAC; MIPS; PACS; SPIRE

[a] Values from Aniano et al. (2011) for the circularized PSFs.

[b] The pixel size in the final-map grids is chosen to Nyquist-sample the PSFs.

[c] Other cameras that can be convolved into the camera PSF (see text for details).

els are fit to the observed intensities. The convolution to a common PSF is carried out using the methods described by Aniano et al. (2011). In the present work, we present, for each galaxy, resolved results at two final-map PSFs: SPIRE250 and MIPS160, henceforth abbreviated as S250 and M160. S250 is the PSF with smallest FWHM (full width at half maximum) that allows use of enough cameras to adequately constrain the dust SED (IRAC, MIPS24, and PACS70, 100, 160, SPIRE250). The M160 PSF allows inclusion of *all* the cameras (IRAC, MIPS, PACS, SPIRE), therefore producing the most reliable maps; this will be our "gold standard". Table 4 lists the resolutions of the cameras, the pixel size in the final-map grids used, and the other cameras that can be used at this resolution. In Appendix D we compare dust mass estimates obtained with different final-map PSFs.

4.3. *Image Segmentation*

After convolution to a common "final-map" PSF and background subtraction, we next fit a dust model to the observed SED of each pixel in the field. In order for dust mass estimation to be reliable, the pixel's SED must be measured in a number of bands with a reasonable signal/noise ratio. However, estimates of the total dust infrared luminosity per unit area from a single pixel, Σ_{Ld}, are reliable so long as there is a significant detection of far-infrared emission after background subtraction.

The procedure used for automatically identifying "galaxy" pixels is described in Appendices A and B of AD12. For purposes of dust mass estimation, we need to limit the modeling to a "galaxy mask" consisting of pixels where the emission from the galaxy of interest has sufficiently high surface brightness for dust mass estimation (via SED fitting) to be reasonably reliable.

A simple criterion for "sufficiently high surface brightness" is that the total dust luminosity/projected area Σ_{Ld} exceed a specified threshold value, $\Sigma_{Ld,\rm min}$. The value chosen for $\Sigma_{Ld,\rm min}$ will depend on the noisiness of the data [which may depend on the brightness of the (subtracted) Galactic foreground emission, as well as on the presence of other extragalactic objects in the field, stars, or even small-scale structure in the Galactic foreground, which may compromise background estimation and subtraction]. The choice of $\Sigma_{Ld,\rm min}$ will also depend on the choice of final-map PSF: use of a larger PSF improves the signal/noise in each pixel by smoothing, and also enables use of more cameras to constrain the dust modeling, and thus may allow use of a lower threshold $\Sigma_{Ld,\rm min}$. In the present study, $\Sigma_{Ld,\rm min}$ was chosen subjectively for each galaxy.

In this paper we report results for two final-map PSFs: S250, and M160, with the PSF FWHM corresponding to linear scales FWHM $= 0.88\,$kpc for S250 and $1.88\,$kpc for M160 at the median distance $D = 10\,$Mpc of the KINGFISH galaxy sample. Table 2 lists $\Sigma_{Ld,\rm min}$ used to define the galaxy masks for the M160 resolution studies, for the 62 galaxies where we detect dust emission. Our adopted values of $\Sigma_{Ld,\rm min}$ vary from galaxy to galaxy, ranging from values as low as $0.58 L_\odot\,\rm pc^{-2}$ (NGC 2915) to values as high as $7 L_\odot\,\rm pc^{-2}$ (NGC 6946). The median $\Sigma_{Ld,\rm min} = 1.6 L_\odot\,\rm pc^{-2}$ (e.g., NGC 4625). For each galaxy where dust is reliably detected at M160 resolution, we also generate a S250 resolution mask, intended to comprise the region where the S250 resolution data permit reliable estimation of the dust surface density. Our S250 masks are often similar in size to the M160 mask, but for some galaxies the S250 mask is considerably smaller than the M160 mask – the most extreme example is NGC 1481, where the S250 mask area is only 37% of M160 mask area. The M160 and S250 masks are shown in Figures 17.1-17.62. The solid angle of each mask is listed in Table 2. Because of the improved signal-to-noise ratio (S/N) in each pixel, most of the analysis in this paper will be done with the M160 resolution images and masks.

For 5 dwarf galaxies where dust detection is uncertain (DDO053, DDO154, DDO165, Hol1, and M81dwB) we choose instead to use masks defined by H I observations. For 3 elliptical galaxies where dust detection is uncertain (NGC0584, NGC0855, and NGC1404) we use $\Sigma_{Ld,\rm min}$-based masks. . We do not detect dust in any of these 8 galaxies. See Appendix B for further details.

4.4. *Integrated Fluxes*

The *Spitzer* and *Herschel* band surface brightnesses are integrated over the M160 and S250 resolution galaxy masks to obtain integrated flux densities. The IRAC and MIPS flux densities are given in Table 5, and the PACS and SPIRE flux densities are given in Table 6. Note that MIPS70, MIPS160, SPIRE350, and SPIRE500 are not used at S250 resolution.

The uncertainties given in Tables 5 and 6 include uncertainties associated with background subtraction, as well as calibration uncertainties. As discussed in §5.3, the fluxes measured by PACS and MIPS sometimes differ by considerably more than the estimated uncertainties: we know that some of the uncertainties have been underestimated, although it is not clear how to improve on our estimates.

Dale et al. (2017) carried out careful foreground star and background galaxy removal tailored for globally integrated photometry. For 44 of the 53 KINGFISH galaxies where we claim dust detections, the SPIRE500 flux for our M160 galaxy mask is within 10% of the global SPIRE500 photometry from Dale et al. (2017). Thus, we are not missing a significant reservoir of dust in the outer parts of the disk.[5]

4.5. *Gas Masses*

For galaxies observed by THINGS, H I 21 cm line intensities were extracted over the area of the M160 resolution galaxy mask for each galaxy. The H I column density $N(\rm H\,I)$ was estimated assuming the 21 cm emission to be optically thin.

For the 38 galaxies in the HERACLES sample, ^{12}CO(2–1) line fluxes were obtained by integrating over the M160 resolution galaxy mask, and the H_2 mass was estimated from the CO $2 \rightarrow 1$ line flux assuming $T_B(2\rightarrow 1)/T_B(1\rightarrow 0) = 0.7$ and a standard conversion factor[6] $X_{\rm CO,1-0} = 2 \times 10^{20} \rm H_2\,cm^{-2}(\,K\,km\,s^{-1})^{-1}$. The adopted $X_{\rm CO}$ value is representative of the values found in 26 nearby star-forming galaxies by Sandstrom et al. (2013).

For NGC 1266 we use the integrated CO emission and the lower bound on the H I mass from Alatalo et al. (2011).

5. DUST MODELING

5.1. *DL07 Dust Model*

We employ the DL07 dust model, using "Milky Way" grain size distributions (Weingartner & Draine 2001a). DL07 described the construction of the dust model, and AD12 described its usage in the context of the KINGFISH galaxies. The DL07 dust model has a mixture of amorphous silicate grains and carbonaceous grains, with a distribution of grain sizes. The distribution of grain sizes was chosen to reproduce the wavelength dependence of interstellar extinction within a few kpc of the Sun (Weingartner & Draine 2001a). The silicate and carbonaceous content of the dust grains was constrained by observations of the gas phase depletions in the ISM. It is assumed that the radiation field heating the dust has a universal spectrum, taken to be that of the local interstellar radiation field estimated by Mathis et al. (1983), scaled by a dimensionless factor U. Following DL07, we assume that in each pixel there is dust exposed to radiation with a single intensity $U_{\rm min}$, and also dust heated by a power-law distribution of starlight intensities with $U_{\rm min} < U < U_{\rm max}$:

$$\frac{dM_{\rm d}}{dU} = (1-\gamma)M_{\rm d}\delta(U-U_{\rm min}) + \gamma M_d \frac{(\alpha-1)U^{-\alpha}}{U_{\rm min}^{1-\alpha} - U_{\rm max}^{1-\alpha}} \quad , \tag{1}$$

where $M_{\rm d}$ is the total dust mass in the pixel, and γ is the fraction of the dust mass that is heated by the power-law distribution of starlight intensities.

The DL07 model has 6 adjustable parameters pertaining to the dust and the starlight heating the dust:

1. $q_{\rm PAH}$: the fraction of the total grain mass contributed by polycyclic aromatic hydrocarbons (PAHs) containing fewer than 10^3 carbon atoms.

2. $U_{\rm min}$: the intensity of the diffuse ISM radiation field heating the dust, relative to the solar neighborhood.

3. α: the exponent of the power-law distribution of heating starlight intensities between $U_{\rm min}$ and $U_{\rm max}$. The case $\alpha = 2$ corresponds to constant dust heating power per logarithmic interval in starlight intensity U; many galaxies seem to be characterized by $\alpha \approx 2$.

4. $U_{\rm max}$: the maximum heating starlight intensity of the power-law distribution of heating starlight intensities.

5. γ: the fraction of the dust mass exposed to the power-law distribution of starlight intensities.

[5] For NGC 1512 Dale et al. (2017) find a SPIRE 500 flux that is 39% larger than our value, but part of the difference is because they included the companion galaxy NGC 1510, which we have treated separately.

[6] $X_{\rm CO,1-0} = 2 \times 10^{20} \rm H_2\,cm^{-2}(\,K\,km\,s^{-1})^{-1}$ corresponds to $\alpha_{\rm CO,1-0} = 4.35 M_\odot\,\rm pc^{-2}(\,K\,km\,s^{-1})^{-1}$ if a factor 1.36 is assumed to allow for Helium and heavier elements.

Table 5. Spitzer Photometry of KINGFISH Galaxies with Dust Detections

		IRAC F_ν(Jy)				MIPS F_ν(Jy)		
Galaxy	mask	3.6μm	4.5μm	5.8μm	8.0μm	24μm	70μm	160μm
Hol2	S250	0.090 ± 0.018	0.065 ± 0.014	0.041 ± 0.015	0.047 ± 0.013	0.187 ± 0.033	—	—
”	M160	0.097 ± 0.024	0.070 ± 0.019	0.042 ± 0.015	0.047 ± 0.014	0.178 ± 0.027	3.1 ± 1.4	3.3 ± 1.9
IC342	S250	14.3 ± 2.3	8.6 ± 1.6	12.0 ± 3.6	$30. \pm 6.$	36.2 ± 4.3	—	—
”	M160	14.3 ± 2.5	8.6 ± 1.5	12.0 ± 3.4	$30. \pm 6.$	36.3 ± 4.1	$338. \pm 161.$	$913. \pm 302.$
IC2574	S250	0.136 ± 0.028	0.101 ± 0.021	0.058 ± 0.023	0.061 ± 0.035	0.27 ± 0.06	—	—
”	M160	0.135 ± 0.035	0.100 ± 0.027	0.057 ± 0.021	0.059 ± 0.029	0.246 ± 0.044	4.8 ± 2.1	9.5 ± 5.0
NGC0337	S250	0.092 ± 0.010	0.065 ± 0.006	0.139 ± 0.035	0.37 ± 0.07	0.76 ± 0.08	—	—
”	M160	0.092 ± 0.015	0.066 ± 0.008	0.137 ± 0.036	0.36 ± 0.07	0.72 ± 0.08	10.1 ± 3.1	16.5 ± 3.9
NGC0628	S250	0.87 ± 0.10	0.60 ± 0.06	1.03 ± 0.25	2.7 ± 0.5	3.18 ± 0.38	—	—
”	M160	0.86 ± 0.11	0.59 ± 0.06	1.00 ± 0.24	2.67 ± 0.48	3.10 ± 0.34	$32. \pm 12.$	$106. \pm 16.$
NGC0925	S250	0.330 ± 0.048	0.226 ± 0.044	0.29 ± 0.08	0.63 ± 0.12	0.85 ± 0.12	—	—
”	M160	0.33 ± 0.06	0.226 ± 0.048	0.28 ± 0.07	0.61 ± 0.12	0.82 ± 0.10	13.0 ± 3.8	$37. \pm 7.$
NGC1097	S250	1.19 ± 0.12	0.79 ± 0.07	1.22 ± 0.29	3.1 ± 0.5	6.5 ± 0.7	—	—
”	M160	1.17 ± 0.13	0.79 ± 0.08	1.19 ± 0.28	3.0 ± 0.5	6.4 ± 0.7	$57. \pm 26.$	$143. \pm 34.$
NGC1266	S250	0.062 ± 0.007	0.048 ± 0.005	0.053 ± 0.014	0.099 ± 0.020	0.88 ± 0.09	—	—
”	M160	0.059 ± 0.008	0.046 ± 0.006	0.051 ± 0.013	0.095 ± 0.019	0.83 ± 0.09	11.5 ± 3.8	9.2 ± 4.1
NGC1291	S250	1.99 ± 0.19	1.24 ± 0.12	0.84 ± 0.23	0.73 ± 0.14	0.53 ± 0.11	—	—
”	M160	1.97 ± 0.20	1.23 ± 0.13	0.82 ± 0.21	0.72 ± 0.14	0.51 ± 0.08	5.7 ± 9.6	$25. \pm 9.$
NGC1316	S250	1.55 ± 0.14	0.98 ± 0.08	0.65 ± 0.15	0.50 ± 0.09	0.353 ± 0.042	—	—
”	M160	1.47 ± 0.14	0.93 ± 0.08	0.62 ± 0.14	0.47 ± 0.09	0.334 ± 0.038	4.8 ± 1.3	9.6 ± 2.3
NGC1377	S250	0.065 ± 0.007	0.092 ± 0.009	0.25 ± 0.06	0.43 ± 0.07	1.79 ± 0.19	—	—
”	M160	0.061 ± 0.008	0.087 ± 0.010	0.24 ± 0.05	0.41 ± 0.07	1.66 ± 0.17	6.0 ± 1.3	2.9 ± 1.0
NGC1482	S250	0.380 ± 0.035	0.271 ± 0.022	0.63 ± 0.14	1.60 ± 0.27	2.33 ± 0.24	—	—
”	M160	0.372 ± 0.042	0.283 ± 0.029	0.60 ± 0.14	1.58 ± 0.27	2.07 ± 0.22	$31. \pm 12.$	$37. \pm 10.$
NGC1512	S250	0.321 ± 0.030	0.207 ± 0.018	0.209 ± 0.049	0.39 ± 0.07	0.42 ± 0.05	—	—
”	M160	0.350 ± 0.042	0.228 ± 0.030	0.22 ± 0.05	0.41 ± 0.07	0.44 ± 0.06	6.1 ± 1.8	20.1 ± 3.8
NGC2146	S250	–	2.11 ± 0.16	–	8.9 ± 1.5	10.4 ± 1.1	—	—
”	M160	–	2.17 ± 0.21	–	8.8 ± 1.6	10.8 ± 1.2	$202. \pm 42.$	$112. \pm 75.$
NGC2798	S250	0.126 ± 0.014	0.091 ± 0.008	0.19 ± 0.06	0.63 ± 0.11	1.54 ± 0.16	—	—
”	M160	0.123 ± 0.018	0.088 ± 0.010	0.18 ± 0.06	0.61 ± 0.11	1.36 ± 0.14	21.8 ± 3.7	$21. \pm 5.$
NGC2841	S250	1.25 ± 0.12	0.77 ± 0.14	0.69 ± 0.18	1.14 ± 0.34	0.96 ± 0.12	—	—
”	M160	1.23 ± 0.12	0.77 ± 0.11	0.68 ± 0.17	1.13 ± 0.25	0.94 ± 0.12	9.9 ± 4.1	$56. \pm 12.$
NGC2915	S250	0.050 ± 0.008	0.033 ± 0.006	0.022 ± 0.008	0.027 ± 0.009	0.056 ± 0.012	—	—
”	M160	0.045 ± 0.010	0.030 ± 0.008	0.019 ± 0.008	0.024 ± 0.007	0.047 ± 0.010	1.12 ± 0.34	0.72 ± 1.21
NGC2976	S250	0.392 ± 0.038	0.267 ± 0.023	0.43 ± 0.10	1.00 ± 0.18	1.40 ± 0.16	—	—
”	M160	0.377 ± 0.042	0.257 ± 0.026	0.41 ± 0.10	0.96 ± 0.17	1.34 ± 0.15	19.0 ± 3.2	$46. \pm 9.$
NGC3049	S250	0.043 ± 0.006	0.0291 ± 0.0049	0.048 ± 0.014	0.120 ± 0.024	0.44 ± 0.05	—	—
”	M160	0.044 ± 0.008	0.031 ± 0.007	0.047 ± 0.013	0.115 ± 0.022	0.404 ± 0.044	2.6 ± 1.3	4.2 ± 1.5
NGC3077	S250	0.52 ± 0.06	0.35 ± 0.05	0.39 ± 0.10	0.85 ± 0.17	1.49 ± 0.17	—	—
”	M160	0.52 ± 0.07	0.35 ± 0.06	0.38 ± 0.10	0.84 ± 0.17	1.36 ± 0.15	18.0 ± 4.3	$32. \pm 8.$
NGC3184	S250	0.52 ± 0.06	0.348 ± 0.040	0.54 ± 0.14	1.37 ± 0.25	1.46 ± 0.18	—	—
”	M160	0.51 ± 0.07	0.341 ± 0.048	0.53 ± 0.14	1.33 ± 0.24	1.42 ± 0.16	$15. \pm 5.$	$63. \pm 13.$
NGC3190	S250	0.340 ± 0.038	0.215 ± 0.028	0.188 ± 0.049	0.29 ± 0.06	0.263 ± 0.033	—	—
”	M160	0.319 ± 0.038	0.203 ± 0.029	0.175 ± 0.045	0.28 ± 0.06	0.245 ± 0.030	4.9 ± 1.5	13.7 ± 2.6
NGC3198	S250	0.273 ± 0.031	0.184 ± 0.022	0.21 ± 0.10	0.67 ± 0.12	1.07 ± 0.12	—	—
”	M160	0.274 ± 0.041	0.185 ± 0.029	0.21 ± 0.09	0.66 ± 0.12	1.03 ± 0.12	9.8 ± 2.8	$35. \pm 8.$
NGC3265	S250	0.0288 ± 0.0041	0.0198 ± 0.0025	0.036 ± 0.010	0.095 ± 0.019	0.291 ± 0.033	—	—
”	M160	0.0273 ± 0.0040	0.0189 ± 0.0031	0.034 ± 0.010	0.090 ± 0.017	0.269 ± 0.029	2.4 ± 0.9	2.5 ± 0.9
NGC3351	S250	0.75 ± 0.07	0.488 ± 0.042	0.58 ± 0.14	1.26 ± 0.23	2.52 ± 0.29	—	—
”	M160	0.74 ± 0.08	0.48 ± 0.05	0.56 ± 0.13	1.23 ± 0.22	2.44 ± 0.26	$21. \pm 8.$	$58. \pm 14.$
NGC3521	S250	1.88 ± 0.18	1.28 ± 0.11	2.10 ± 0.49	5.8 ± 1.0	5.6 ± 0.6	—	—
”	M160	1.86 ± 0.19	1.28 ± 0.12	2.07 ± 0.48	5.7 ± 1.0	5.5 ± 0.6	$64. \pm 22.$	$203. \pm 39.$
NGC3621	S250	1.62 ± 0.24	1.18 ± 0.13	2.2 ± 0.6	4.0 ± 0.7	3.63 ± 0.43	—	—
”	M160	1.62 ± 0.27	1.18 ± 0.15	2.1 ± 0.6	4.0 ± 0.7	3.60 ± 0.41	$46. \pm 13.$	$122. \pm 25.$
NGC3627	S250	1.86 ± 0.17	1.28 ± 0.10	2.06 ± 0.47	5.3 ± 0.9	7.5 ± 0.8	—	—
”	M160	1.88 ± 0.20	1.29 ± 0.13	2.04 ± 0.48	5.2 ± 0.9	7.4 ± 0.8	$88. \pm 27.$	$218. \pm 35.$
NGC3773	S250	0.0236 ± 0.0031	0.0157 ± 0.0021	0.020 ± 0.006	0.046 ± 0.011	0.143 ± 0.019	—	—
”	M160	0.0218 ± 0.0036	0.0146 ± 0.0027	0.019 ± 0.005	0.043 ± 0.009	0.129 ± 0.015	1.4 ± 0.5	1.8 ± 0.9
NGC3938	S250	0.313 ± 0.033	0.213 ± 0.021	0.38 ± 0.09	0.99 ± 0.17	1.10 ± 0.13	—	—
”	M160	0.308 ± 0.040	0.211 ± 0.026	0.37 ± 0.09	0.96 ± 0.17	1.06 ± 0.12	13.2 ± 4.3	$46. \pm 10.$
NGC4236	S250	0.22 ± 0.06	0.155 ± 0.047	0.092 ± 0.098	0.15 ± 0.06	0.51 ± 0.08	—	—
”	M160	0.21 ± 0.06	0.150 ± 0.047	0.087 ± 0.072	0.145 ± 0.048	0.48 ± 0.07	7.8 ± 5.2	$16. \pm 5.$

Table 5. Spitzer Photometry of KINGFISH Galaxies with Dust Detections, contd.

		IRAC F_ν(Jy)				MIPS F_ν(Jy)		
Galaxy	mask	3.6μm	4.5μm	5.8μm	8.0μm	24μm	70μm	160μm
NGC4254	S250	0.68 ± 0.06	0.48 ± 0.09	1.29 ± 0.30	3.9 ± 0.7	4.23 ± 0.45	—	—
”	M160	0.68 ± 0.07	0.47 ± 0.11	1.26 ± 0.29	3.8 ± 0.8	4.11 ± 0.45	$46. \pm 14.$	$127. \pm 23.$
NGC4321	S250	0.88 ± 0.09	0.589 ± 0.048	1.04 ± 0.24	2.86 ± 0.49	3.39 ± 0.36	—	—
”	M160	0.89 ± 0.11	0.60 ± 0.06	1.03 ± 0.25	2.81 ± 0.49	3.33 ± 0.35	$38. \pm 11.$	$126. \pm 26.$
NGC4536	S250	0.394 ± 0.040	0.293 ± 0.026	0.55 ± 0.14	1.61 ± 0.29	3.43 ± 0.37	—	—
”	M160	0.389 ± 0.048	0.295 ± 0.039	0.53 ± 0.13	1.59 ± 0.29	3.30 ± 0.35	$30. \pm 13.$	$54. \pm 11.$
NGC4559	S250	0.402 ± 0.043	0.280 ± 0.029	0.38 ± 0.09	0.84 ± 0.15	1.13 ± 0.14	—	—
”	M160	0.388 ± 0.047	0.271 ± 0.033	0.37 ± 0.09	0.81 ± 0.14	1.07 ± 0.12	15.7 ± 4.0	$46. \pm 9.$
NGC4569	S250	0.65 ± 0.06	0.421 ± 0.034	0.47 ± 0.11	0.98 ± 0.17	1.41 ± 0.16	—	—
”	M160	0.61 ± 0.06	0.395 ± 0.034	0.44 ± 0.10	0.92 ± 0.16	1.32 ± 0.14	10.8 ± 3.9	$37. \pm 7.$
NGC4579	S250	0.76 ± 0.07	0.490 ± 0.041	0.44 ± 0.11	0.70 ± 0.13	0.79 ± 0.09	—	—
”	M160	0.74 ± 0.08	0.475 ± 0.043	0.43 ± 0.10	0.68 ± 0.13	0.75 ± 0.08	8.9 ± 2.1	$36. \pm 6.$
NGC4594	S250	3.26 ± 0.31	2.04 ± 0.17	1.38 ± 0.33	1.22 ± 0.24	0.71 ± 0.09	—	—
”	M160	3.14 ± 0.30	1.96 ± 0.17	1.33 ± 0.31	1.17 ± 0.23	0.68 ± 0.08	7.4 ± 2.6	$36. \pm 7.$
NGC4625	S250	0.045 ± 0.005	0.0296 ± 0.0034	0.050 ± 0.015	0.126 ± 0.023	0.132 ± 0.017	—	—
”	M160	0.044 ± 0.007	0.0291 ± 0.0048	0.049 ± 0.015	0.119 ± 0.022	0.122 ± 0.015	1.83 ± 0.48	4.7 ± 1.2
NGC4631	S250	1.20 ± 0.11	0.85 ± 0.07	2.2 ± 0.5	5.8 ± 1.0	8.0 ± 0.8	—	—
”	M160	1.22 ± 0.14	0.88 ± 0.08	2.2 ± 0.5	5.9 ± 1.0	8.0 ± 0.8	$134. \pm 21.$	$265. \pm 47.$
NGC4725	S250	1.03 ± 0.10	0.66 ± 0.06	0.60 ± 0.16	1.02 ± 0.18	0.85 ± 0.12	—	—
”	M160	1.03 ± 0.11	0.65 ± 0.07	0.60 ± 0.15	1.00 ± 0.18	0.83 ± 0.10	8.5 ± 4.3	$51. \pm 9.$
NGC4736	S250	3.29 ± 0.36	2.14 ± 0.21	2.3 ± 0.6	4.8 ± 0.9	5.6 ± 0.6	—	—
”	M160	3.26 ± 0.36	2.12 ± 0.22	2.3 ± 0.6	4.8 ± 0.8	5.5 ± 0.6	$92. \pm 29.$	$163. \pm 29.$
NGC4826	S250	2.05 ± 0.18	1.31 ± 0.10	1.22 ± 0.28	2.04 ± 0.35	2.46 ± 0.26	—	—
”	M160	2.19 ± 0.21	1.40 ± 0.11	1.25 ± 0.29	2.05 ± 0.35	2.43 ± 0.26	$52. \pm 9.$	$85. \pm 22.$
NGC5055	S250	2.25 ± 0.20	1.51 ± 0.12	2.3 ± 0.6	5.7 ± 1.0	5.7 ± 0.6	—	—
”	M160	2.28 ± 0.22	1.52 ± 0.13	2.3 ± 0.6	5.7 ± 1.0	5.7 ± 0.6	$73. \pm 14.$	$269. \pm 44.$
NGC5398	S250	0.038 ± 0.007	0.027 ± 0.005	0.029 ± 0.009	0.058 ± 0.011	0.260 ± 0.029	—	—
”	M160	0.039 ± 0.010	0.027 ± 0.008	0.029 ± 0.009	0.055 ± 0.012	0.240 ± 0.027	1.8 ± 0.7	2.6 ± 1.0
NGC5408	S250	0.082 ± 0.021	0.064 ± 0.012	0.041 ± 0.021	0.039 ± 0.010	0.403 ± 0.044	—	—
”	M160	0.082 ± 0.038	0.064 ± 0.021	0.042 ± 0.036	0.039 ± 0.014	0.370 ± 0.043	3.0 ± 0.6	1.8 ± 0.8
NGC5457	S250	2.73 ± 0.39	1.83 ± 0.26	3.1 ± 0.9	7.6 ± 1.4	10.9 ± 1.3	—	—
”	M160	2.74 ± 0.41	1.84 ± 0.27	3.1 ± 0.9	7.6 ± 1.4	10.9 ± 1.2	$123. \pm 33.$	$410. \pm 82.$
NGC5474	S250	0.101 ± 0.012	0.069 ± 0.008	0.082 ± 0.026	0.103 ± 0.025	0.160 ± 0.026	—	—
”	M160	0.101 ± 0.015	0.067 ± 0.010	0.082 ± 0.024	0.101 ± 0.022	0.151 ± 0.021	3.4 ± 1.4	8.7 ± 2.5
NGC5713	S250	0.198 ± 0.020	0.136 ± 0.018	0.39 ± 0.09	1.13 ± 0.20	2.38 ± 0.25	—	—
”	M160	0.205 ± 0.029	0.137 ± 0.025	0.40 ± 0.10	1.09 ± 0.19	2.35 ± 0.25	$23. \pm 8.$	$38. \pm 10.$
NGC5866	S250	0.61 ± 0.05	0.390 ± 0.030	0.26 ± 0.06	0.285 ± 0.050	0.214 ± 0.026	—	—
”	M160	0.55 ± 0.05	0.355 ± 0.029	0.24 ± 0.06	0.265 ± 0.046	0.195 ± 0.022	7.8 ± 1.4	16.5 ± 4.0
NGC6946	S250	3.4 ± 0.5	2.44 ± 0.32	5.2 ± 1.3	13.8 ± 2.5	19.7 ± 2.1	—	—
”	M160	3.4 ± 0.6	2.41 ± 0.38	5.1 ± 1.3	13.6 ± 2.4	19.4 ± 2.1	$202. \pm 59.$	$438. \pm 98.$
NGC7331	S250	1.51 ± 0.16	1.00 ± 0.09	1.59 ± 0.37	4.0 ± 0.7	4.04 ± 0.43	—	—
”	M160	1.52 ± 0.20	1.01 ± 0.11	1.54 ± 0.37	3.8 ± 0.7	3.91 ± 0.41	$58. \pm 13.$	$155. \pm 35.$
NGC7793	S250	0.74 ± 0.09	0.503 ± 0.045	0.81 ± 0.21	1.90 ± 0.34	2.12 ± 0.25	—	—
”	M160	0.74 ± 0.10	0.50 ± 0.06	0.80 ± 0.21	1.88 ± 0.33	2.09 ± 0.23	$33. \pm 8.$	$108. \pm 22.$
IC3583	S250	0.037 ± 0.005	0.0237 ± 0.0030	0.019 ± 0.007	0.034 ± 0.009	0.048 ± 0.010	—	—
”	M160	0.034 ± 0.007	0.0224 ± 0.0040	0.017 ± 0.005	0.033 ± 0.008	0.045 ± 0.007	0.84 ± 0.31	1.8 ± 0.7
NGC0586	S250	0.00063 ± 0.00221	0.00031 ± 0.00132	$-.0006 \pm 0.0031$	$-.0001 \pm 0.0032$	0.029 ± 0.006	—	—
”	M160	0.00061 ± 0.00563	0.00051 ± 0.00264	$-.0002 \pm 0.0026$	$-.0000 \pm 0.0021$	0.0254 ± 0.0041	0.36 ± 0.33	1.3 ± 0.6
NGC1317	S250	0.262 ± 0.028	0.164 ± 0.017	0.159 ± 0.040	0.269 ± 0.049	0.253 ± 0.030	—	—
”	M160	0.248 ± 0.030	0.156 ± 0.020	0.149 ± 0.037	0.253 ± 0.046	0.234 ± 0.027	5.1 ± 1.1	10.6 ± 2.6
NGC1481	S250	0.0148 ± 0.0025	–	0.0132 ± 0.0041	–	0.050 ± 0.007	—	—
”	M160	0.019 ± 0.007	–	0.016 ± 0.007	–	0.052 ± 0.008	0.62 ± 0.74	0.73 ± 0.46
NGC1510	S250	0.0149 ± 0.0017	0.0106 ± 0.0011	0.0102 ± 0.0027	0.0193 ± 0.0037	0.127 ± 0.014	—	—
”	M160	0.024 ± 0.005	0.0172 ± 0.0046	0.0133 ± 0.0043	0.024 ± 0.006	0.134 ± 0.016	1.08 ± 0.48	1.3 ± 0.5
NGC3187	S250	0.0249 ± 0.0048	0.019 ± 0.005	0.030 ± 0.009	0.064 ± 0.014	0.101 ± 0.014	—	—
”	M160	0.027 ± 0.010	0.021 ± 0.010	0.029 ± 0.010	0.061 ± 0.018	0.093 ± 0.013	1.25 ± 0.46	3.8 ± 1.1
NGC4533	S250	0.0158 ± 0.0023	0.0100 ± 0.0017	0.0088 ± 0.0047	0.022 ± 0.006	0.030 ± 0.007	—	—
”	M160	0.0165 ± 0.0042	0.0098 ± 0.0026	0.0067 ± 0.0047	0.021 ± 0.007	0.029 ± 0.007	0.51 ± 0.35	1.1 ± 0.8
NGC7335	S250	0.047 ± 0.007	0.0305 ± 0.0034	0.021 ± 0.006	0.027 ± 0.006	0.0299 ± 0.0049	—	—
”	M160	0.040 ± 0.008	0.0260 ± 0.0043	0.020 ± 0.006	0.027 ± 0.006	0.0294 ± 0.0046	0.54 ± 0.17	1.6 ± 0.5
NGC7337	S250	0.0278 ± 0.0040	0.0179 ± 0.0022	0.0135 ± 0.0040	0.0215 ± 0.0045	0.0201 ± 0.0035	—	—
”	M160	0.024 ± 0.006	0.0156 ± 0.0036	0.0117 ± 0.0042	0.019 ± 0.005	0.0171 ± 0.0031	0.33 ± 0.25	0.89 ± 0.40

Table 6. Herschel Photometry of KINGFISH Galaxies with Dust Detections

		PACS F_ν (Jy)			SPIRE F_ν (Jy)		
Galaxy	mask	70μm	100μm	160μm	250μm	350μm	500μm
Hol2	S250	4.3 ± 3.1	4.2 ± 3.7	3.2 ± 2.5	1.8 ± 0.5	–	–
”	M160	4.1 ± 2.4	4.0 ± 2.9	2.9 ± 2.0	1.70 ± 0.39	0.96 ± 0.25	0.44 ± 0.14
IC342	S250	$465. \pm 230.$	$904. \pm 402.$	$1108. \pm 325.$	$587. \pm 81.$	–	–
”	M160	$462. \pm 196.$	$901. \pm 336.$	$1101. \pm 293.$	$584. \pm 81.$	$262. \pm 37.$	$97. \pm 14.$
IC2574	S250	5.8 ± 5.9	6.6 ± 7.0	8.5 ± 5.7	6.4 ± 1.7	–	–
”	M160	5.4 ± 4.2	6.0 ± 4.8	7.9 ± 4.7	6.0 ± 1.3	3.9 ± 0.8	1.79 ± 0.44
NGC0337	S250	13.8 ± 3.9	$21. \pm 6.$	19.8 ± 4.0	8.4 ± 1.1	–	–
”	M160	12.9 ± 3.7	$20. \pm 6.$	18.6 ± 3.6	7.8 ± 1.1	3.6 ± 0.6	1.42 ± 0.23
NGC0628	S250	$41. \pm 18.$	$81. \pm 27.$	$113. \pm 19.$	$61. \pm 8.$	–	–
”	M160	$40. \pm 15.$	$79. \pm 22.$	$109. \pm 17.$	$59. \pm 7.$	27.5 ± 3.3	10.6 ± 1.4
NGC0925	S250	$15. \pm 8.$	$29. \pm 11.$	$37. \pm 8.$	24.4 ± 3.2	–	–
”	M160	$15. \pm 6.$	$27. \pm 9.$	$36. \pm 7.$	23.1 ± 2.8	13.1 ± 1.6	5.9 ± 0.8
NGC1097	S250	$79. \pm 36.$	$126. \pm 56.$	$134. \pm 36.$	$67. \pm 8.$	–	–
”	M160	$78. \pm 29.$	$124. \pm 48.$	$131. \pm 35.$	$65. \pm 7.$	28.5 ± 3.2	10.3 ± 1.3
NGC1266	S250	$16. \pm 6.$	$18. \pm 8.$	$12. \pm 5.$	4.4 ± 0.6	–	–
”	M160	14.5 ± 4.4	$17. \pm 7.$	11.2 ± 4.1	4.1 ± 0.5	1.59 ± 0.23	0.52 ± 0.10
NGC1291	S250	4.6 ± 24.9	8.4 ± 27.6	$24. \pm 18.$	16.3 ± 3.9	–	–
”	M160	4.4 ± 18.2	8.3 ± 18.1	$23. \pm 13.$	15.7 ± 2.5	8.6 ± 1.5	3.4 ± 0.9
NGC1316	S250	5.3 ± 2.4	9.9 ± 3.9	10.8 ± 2.7	4.8 ± 0.7	–	–
”	M160	5.0 ± 1.9	9.3 ± 3.4	10.2 ± 2.5	4.6 ± 0.6	1.88 ± 0.28	0.66 ± 0.13
NGC1377	S250	7.6 ± 2.6	6.9 ± 3.0	3.9 ± 1.5	1.37 ± 0.29	–	–
”	M160	7.0 ± 1.7	6.3 ± 2.2	3.6 ± 1.2	1.22 ± 0.18	0.50 ± 0.09	0.171 ± 0.050
NGC1482	S250	$43. \pm 17.$	$54. \pm 23.$	$43. \pm 10.$	15.4 ± 1.8	–	–
”	M160	$41. \pm 13.$	$52. \pm 19.$	$41. \pm 10.$	14.6 ± 1.6	5.5 ± 0.7	1.64 ± 0.29
NGC1512	S250	7.0 ± 2.2	13.7 ± 3.8	18.3 ± 3.2	10.2 ± 1.3	–	–
”	M160	7.2 ± 3.1	12.9 ± 4.1	18.6 ± 4.0	11.2 ± 1.4	5.6 ± 0.8	2.22 ± 0.36
NGC2146	S250	$200. \pm 37.$	$242. \pm 140.$	$182. \pm 96.$	$63. \pm 7.$	–	–
”	M160	$194. \pm 42.$	$235. \pm 105.$	$176. \pm 75.$	$62. \pm 7.$	22.6 ± 2.5	7.2 ± 0.9
NGC2798	S250	$26. \pm 7.$	$30. \pm 10.$	21.9 ± 5.0	8.1 ± 1.0	–	–
”	M160	24.6 ± 4.5	$28. \pm 8.$	$20. \pm 5.$	7.6 ± 0.9	2.88 ± 0.36	0.89 ± 0.16
NGC2841	S250	$11. \pm 10.$	$29. \pm 15.$	$50. \pm 13.$	33.9 ± 4.5	–	–
”	M160	$11. \pm 8.$	$28. \pm 11.$	$48. \pm 13.$	32.9 ± 3.8	15.9 ± 1.9	6.3 ± 0.9
NGC2915	S250	1.1 ± 0.7	2.0 ± 1.4	1.8 ± 1.2	0.62 ± 0.23	–	–
”	M160	0.98 ± 0.52	1.7 ± 1.2	1.5 ± 1.1	0.46 ± 0.24	0.24 ± 0.13	0.098 ± 0.062
NGC2976	S250	$22. \pm 6.$	$38. \pm 9.$	$47. \pm 9.$	24.6 ± 3.1	–	–
”	M160	20.6 ± 4.5	$36. \pm 8.$	$45. \pm 9.$	23.6 ± 3.1	11.4 ± 1.5	4.4 ± 0.6
NGC3049	S250	4.0 ± 2.2	5.7 ± 3.1	5.4 ± 2.0	2.78 ± 0.44	–	–
”	M160	3.7 ± 1.7	5.1 ± 2.4	4.9 ± 1.5	2.45 ± 0.32	1.32 ± 0.18	0.67 ± 0.10
NGC3077	S250	$21. \pm 7.$	$30. \pm 11.$	$30. \pm 8.$	15.3 ± 2.2	–	–
”	M160	$20. \pm 6.$	$29. \pm 9.$	$29. \pm 8.$	15.0 ± 2.0	7.3 ± 1.0	2.94 ± 0.46
NGC3184	S250	$18. \pm 13.$	$39. \pm 17.$	$55. \pm 15.$	33.4 ± 4.6	–	–
”	M160	$18. \pm 9.$	$38. \pm 13.$	$54. \pm 13.$	32.3 ± 3.8	15.3 ± 1.9	5.8 ± 0.9
NGC3190	S250	6.5 ± 2.9	12.0 ± 4.1	15.7 ± 3.7	8.5 ± 1.1	–	–
”	M160	5.9 ± 2.3	11.2 ± 3.3	14.6 ± 2.8	7.9 ± 0.9	3.39 ± 0.41	1.16 ± 0.18
NGC3198	S250	11.7 ± 4.4	$24. \pm 9.$	$31. \pm 8.$	18.6 ± 2.3	–	–
”	M160	11.4 ± 3.8	$23. \pm 9.$	$29. \pm 8.$	17.8 ± 2.1	9.3 ± 1.1	3.9 ± 0.5
NGC3265	S250	3.5 ± 1.6	3.7 ± 2.0	2.9 ± 1.2	1.26 ± 0.25	–	–
”	M160	3.2 ± 1.2	3.4 ± 1.7	2.6 ± 1.0	1.15 ± 0.16	0.51 ± 0.09	0.199 ± 0.047
NGC3351	S250	$27. \pm 14.$	$50. \pm 23.$	$55. \pm 17.$	31.9 ± 4.0	–	–
”	M160	$26. \pm 11.$	$48. \pm 18.$	$53. \pm 15.$	30.8 ± 3.5	13.8 ± 1.6	4.8 ± 0.7
NGC3521	S250	$83. \pm 28.$	$168. \pm 51.$	$210. \pm 36.$	$108. \pm 12.$	–	–
”	M160	$81. \pm 26.$	$165. \pm 48.$	$206. \pm 38.$	$107. \pm 12.$	$46. \pm 5.$	16.6 ± 2.1
NGC3621	S250	$52. \pm 20.$	$100. \pm 32.$	$130. \pm 27.$	$67. \pm 9.$	–	–
”	M160	$51. \pm 18.$	$98. \pm 27.$	$128. \pm 26.$	$67. \pm 8.$	31.7 ± 3.8	12.8 ± 1.7
NGC3627	S250	$109. \pm 32.$	$192. \pm 56.$	$201. \pm 30.$	$92. \pm 10.$	–	–
”	M160	$107. \pm 31.$	$190. \pm 55.$	$198. \pm 37.$	$92. \pm 10.$	37.0 ± 4.2	12.4 ± 1.6
NGC3773	S250	1.5 ± 1.1	2.2 ± 1.5	2.4 ± 1.2	1.06 ± 0.22	–	–
”	M160	1.3 ± 0.8	2.0 ± 1.2	2.1 ± 0.9	0.92 ± 0.14	0.42 ± 0.07	0.148 ± 0.043
NGC3938	S250	$16. \pm 8.$	$30. \pm 12.$	$41. \pm 10.$	22.9 ± 3.0	–	–
”	M160	$15. \pm 6.$	$29. \pm 10.$	$39. \pm 10.$	22.1 ± 2.6	10.1 ± 1.2	3.8 ± 0.5
NGC4236	S250	7.4 ± 10.2	$11. \pm 13.$	$16. \pm 8.$	10.8 ± 2.3	–	–
”	M160	6.7 ± 8.0	$10. \pm 10.$	$14. \pm 6.$	10.2 ± 1.5	6.5 ± 1.0	3.3 ± 0.6

Table 6. Herschel Photometry of KINGFISH Galaxies with Dust Detections, contd.

		PACS F_ν(Jy)			SPIRE F_ν(Jy)		
Galaxy	mask	70μm	100μm	160μm	250μm	350μm	500μm
NGC4254	S250	$61. \pm 18.$	$113. \pm 30.$	$129. \pm 21.$	$62. \pm 7.$	–	–
”	M160	$59. \pm 17.$	$110. \pm 30.$	$125. \pm 23.$	$61. \pm 7.$	24.7 ± 2.8	8.3 ± 1.0
NGC4321	S250	$45. \pm 15.$	$90. \pm 27.$	$118. \pm 25.$	$63. \pm 7.$	–	–
”	M160	$45. \pm 14.$	$88. \pm 26.$	$115. \pm 27.$	$62. \pm 7.$	26.8 ± 3.1	9.2 ± 1.2
NGC4536	S250	$41. \pm 17.$	$57. \pm 22.$	$56. \pm 11.$	26.8 ± 3.1	–	–
”	M160	$40. \pm 15.$	$55. \pm 19.$	$54. \pm 11.$	25.9 ± 2.9	11.6 ± 1.4	4.5 ± 0.6
NGC4559	S250	$19. \pm 6.$	$35. \pm 11.$	$43. \pm 9.$	25.0 ± 3.1	–	–
”	M160	18.3 ± 4.9	$34. \pm 9.$	$41. \pm 9.$	24.0 ± 2.9	12.6 ± 1.5	5.5 ± 0.7
NGC4569	S250	$15. \pm 6.$	$32. \pm 11.$	$40. \pm 7.$	20.8 ± 2.4	–	–
”	M160	14.0 ± 4.5	$30. \pm 9.$	$38. \pm 7.$	19.5 ± 2.1	8.2 ± 0.9	2.81 ± 0.36
NGC4579	S250	10.6 ± 3.9	$27. \pm 7.$	$35. \pm 6.$	19.7 ± 2.3	–	–
”	M160	10.2 ± 3.1	$25. \pm 6.$	$33. \pm 6.$	18.7 ± 2.1	8.2 ± 0.9	2.88 ± 0.39
NGC4594	S250	8.4 ± 4.4	$26. \pm 9.$	$38. \pm 7.$	23.5 ± 2.8	–	–
”	M160	7.9 ± 3.5	$25. \pm 8.$	$36. \pm 7.$	22.4 ± 2.6	10.8 ± 1.3	4.3 ± 0.6
NGC4625	S250	1.7 ± 1.0	3.8 ± 2.0	4.9 ± 1.4	2.49 ± 0.38	–	–
”	M160	1.6 ± 0.8	3.5 ± 1.6	4.4 ± 1.4	2.28 ± 0.28	1.11 ± 0.15	0.47 ± 0.09
NGC4631	S250	$141. \pm 27.$	$235. \pm 48.$	$244. \pm 37.$	$116. \pm 12.$	–	–
”	M160	$139. \pm 25.$	$232. \pm 49.$	$243. \pm 47.$	$117. \pm 12.$	$53. \pm 6.$	20.6 ± 2.4
NGC4725	S250	$11. \pm 7.$	$27. \pm 12.$	$47. \pm 10.$	30.5 ± 3.9	–	–
”	M160	$11. \pm 6.$	$26. \pm 10.$	$45. \pm 10.$	29.9 ± 3.6	15.5 ± 1.9	6.3 ± 0.9
NGC4736	S250	$109. \pm 43.$	$170. \pm 60.$	$151. \pm 30.$	$65. \pm 9.$	–	–
”	M160	$108. \pm 35.$	$168. \pm 52.$	$148. \pm 30.$	$64. \pm 7.$	26.2 ± 3.4	9.1 ± 1.4
NGC4826	S250	$57. \pm 13.$	$97. \pm 28.$	$92. \pm 24.$	38.2 ± 4.1	–	–
”	M160	$55. \pm 11.$	$95. \pm 24.$	$91. \pm 22.$	38.1 ± 4.1	15.2 ± 1.8	5.1 ± 0.7
NGC5055	S250	$82. \pm 21.$	$183. \pm 42.$	$249. \pm 42.$	$138. \pm 15.$	–	–
”	M160	$82. \pm 18.$	$180. \pm 39.$	$245. \pm 46.$	$137. \pm 15.$	$60. \pm 7.$	21.7 ± 2.5
NGC5398	S250	2.6 ± 1.4	3.4 ± 1.8	2.8 ± 1.1	1.74 ± 0.30	–	–
”	M160	2.3 ± 1.1	3.2 ± 1.7	2.5 ± 1.1	1.59 ± 0.22	0.87 ± 0.13	0.41 ± 0.08
NGC5408	S250	3.5 ± 1.2	3.3 ± 1.5	2.2 ± 0.9	0.80 ± 0.21	–	–
”	M160	3.1 ± 1.0	2.9 ± 1.2	2.0 ± 0.8	0.71 ± 0.14	0.37 ± 0.08	0.123 ± 0.049
NGC5457	S250	$136. \pm 56.$	$268. \pm 93.$	$348. \pm 82.$	$203. \pm 26.$	–	–
”	M160	$136. \pm 45.$	$267. \pm 80.$	$347. \pm 82.$	$202. \pm 23.$	$100. \pm 12.$	$41. \pm 5.$
NGC5474	S250	4.4 ± 3.3	8.0 ± 4.9	7.7 ± 3.2	4.8 ± 0.8	–	–
”	M160	4.3 ± 2.6	7.9 ± 4.4	7.1 ± 2.8	4.6 ± 0.6	2.64 ± 0.38	1.23 ± 0.21
NGC5713	S250	$30. \pm 9.$	$44. \pm 15.$	$41. \pm 10.$	16.3 ± 1.9	–	–
”	M160	$28. \pm 10.$	$42. \pm 14.$	$40. \pm 10.$	16.6 ± 2.0	6.8 ± 0.9	2.28 ± 0.39
NGC5866	S250	9.2 ± 3.2	$18. \pm 6.$	18.2 ± 4.5	7.8 ± 0.9	–	–
”	M160	8.4 ± 2.0	16.7 ± 4.5	16.7 ± 4.1	7.1 ± 0.8	2.89 ± 0.34	0.94 ± 0.14
NGC6946	S250	$260. \pm 75.$	$465. \pm 136.$	$531. \pm 112.$	$249. \pm 29.$	–	–
”	M160	$255. \pm 63.$	$455. \pm 116.$	$519. \pm 100.$	$244. \pm 28.$	$101. \pm 12.$	35.2 ± 4.3
NGC7331	S250	$68. \pm 16.$	$138. \pm 35.$	$175. \pm 35.$	$89. \pm 10.$	–	–
”	M160	$65. \pm 15.$	$133. \pm 33.$	$169. \pm 35.$	$87. \pm 9.$	38.3 ± 4.2	14.2 ± 1.6
NGC7793	S250	$36. \pm 14.$	$71. \pm 24.$	$91. \pm 23.$	$54. \pm 7.$	–	–
”	M160	$36. \pm 13.$	$70. \pm 23.$	$89. \pm 23.$	$53. \pm 6.$	27.9 ± 3.2	11.9 ± 1.5
IC3583	S250	1.1 ± 0.7	2.0 ± 1.1	2.1 ± 0.7	1.27 ± 0.24	–	–
”	M160	0.96 ± 0.54	1.8 ± 0.9	2.0 ± 0.7	1.16 ± 0.19	0.62 ± 0.10	0.25 ± 0.06
NGC0586	S250	0.29 ± 0.62	0.85 ± 0.91	1.4 ± 0.6	0.92 ± 0.18	–	–
”	M160	0.27 ± 0.46	0.76 ± 0.72	1.2 ± 0.6	0.80 ± 0.12	0.38 ± 0.07	0.130 ± 0.035
NGC1317	S250	6.1 ± 1.9	10.9 ± 3.3	11.1 ± 2.8	5.0 ± 0.7	–	–
”	M160	5.6 ± 1.4	10.2 ± 3.0	10.3 ± 2.7	4.6 ± 0.6	1.88 ± 0.24	0.64 ± 0.10
NGC1481	S250	1.0 ± 0.5	1.0 ± 0.5	0.88 ± 0.33	0.41 ± 0.08	–	–
”	M160	1.3 ± 0.9	0.93 ± 0.81	0.73 ± 0.54	0.42 ± 0.08	0.183 ± 0.049	0.024 ± 0.034
NGC1510	S250	1.12 ± 0.27	1.19 ± 0.32	0.97 ± 0.25	0.43 ± 0.07	–	–
”	M160	1.5 ± 0.8	1.3 ± 0.8	1.3 ± 0.6	0.78 ± 0.15	0.44 ± 0.09	0.22 ± 0.06
NGC3187	S250	1.5 ± 1.0	2.6 ± 1.3	3.9 ± 1.1	2.47 ± 0.36	–	–
”	M160	1.4 ± 0.9	2.2 ± 1.2	3.6 ± 1.2	2.32 ± 0.31	1.33 ± 0.18	0.63 ± 0.11
NGC4533	S250	0.43 ± 0.49	1.4 ± 0.8	1.6 ± 0.6	0.95 ± 0.16	–	–
”	M160	0.50 ± 0.61	1.3 ± 0.7	1.5 ± 0.7	0.82 ± 0.14	0.40 ± 0.08	0.190 ± 0.043
NGC7335	S250	0.60 ± 0.44	1.5 ± 0.7	1.7 ± 0.5	1.03 ± 0.17	–	–
”	M160	0.56 ± 0.29	1.3 ± 0.6	1.5 ± 0.5	0.91 ± 0.15	0.42 ± 0.07	0.171 ± 0.034
NGC7337	S250	0.17 ± 0.33	0.62 ± 0.62	0.81 ± 0.39	0.69 ± 0.11	–	–
”	M160	0.14 ± 0.35	0.46 ± 0.51	0.67 ± 0.39	0.57 ± 0.10	0.27 ± 0.05	0.097 ± 0.022

6. $M_{\rm d}$: the dust mass in the pixel.

   In addition, for modeling the observed fluxes in the IRAC bands, we have an additional adjustable parameter (see AD12):

7. $\Omega_\star$: the solid angle subtended by stars within the pixel, determined from the "direct" starlight intensity in the infrared, i.e., starlight that directly contributes to the IRAC photometry, without warming the dust.

The mean starlight intensity seen by the dust is

$$\bar{U} = (1-\gamma)U_{\rm min} + \gamma\frac{(\alpha-1)}{(2-\alpha)}\frac{U_{\rm max}^{2-\alpha}-U_{\rm min}^{2-\alpha}}{U_{\rm min}^{1-\alpha}-U_{\rm max}^{1-\alpha}} \quad \text{if } \alpha\neq 2, \tag{2}$$

$$= (1-\gamma)U_{\rm min} + \gamma U_{\rm min}\frac{\ln(U_{\rm max}/U_{\rm min})}{1-(U_{\rm min}/U_{\rm max})} \quad \text{if } \alpha = 2. \tag{3}$$

The parameter γ is directly related to $f_{\rm PDR}$, defined to be the fraction of the total dust luminosity $L_{\rm d}$ that is radiated by dust in regions where $U > 10^2$:

$$f_{\rm PDR} = \frac{\gamma\left[1-\left(\frac{100}{U_{\rm max}}\right)^{2-\alpha}\right]}{(1-\gamma)\frac{(2-\alpha)}{(\alpha-1)}\left(\frac{U_{\rm min}}{U_{\rm max}}\right)^{2-\alpha}\left[1-\left(\frac{U_{\rm min}}{U_{\rm max}}\right)^{\alpha-1}\right]+\gamma\left[1-\left(\frac{U_{\rm min}}{U_{\rm max}}\right)^{2-\alpha}\right]}$$

if $\alpha\neq 2$, or

$$f_{\rm PDR} = \frac{\gamma\ln\left(\frac{U_{\rm max}}{100}\right)}{(1-\gamma)\left(1-\frac{U_{\rm min}}{U_{\rm max}}\right)+\gamma\ln\left(\frac{U_{\rm max}}{U_{\rm min}}\right)} \quad \text{if } \alpha = 2\ . \tag{4}$$

For each set of dust parameters $(M_{\rm d}, q_{\rm PAH}, \gamma, U_{\rm min}, U_{\rm max}, \alpha)$, and the adopted grain size distribution and grain properties, the dust emission spectrum is computed from first principles. The observed SEDs are consistent with models having $U_{\rm max} = 10^7$, and we therefore fix $U_{\rm max} \equiv 10^7$. Moreover, the model emission is linear in $M_{\rm d}$, $L_\star$, and γ (or, equivalently, $f_{\rm PDR}$), so in the dust fitting algorithms we only need to explore a three dimensional parameter space ($q_{\rm PAH}$, $U_{\rm min}$, and α). The limits on adjustable parameters are given in Table 7. The allowed range for $U_{\rm min}$ is determined by the wavelength coverage of the data used in the fit.

The region observed is at a distance D from the observer and Ω_j is the solid angle of pixel j. For each pixel j, the best-fit model vector $\{L_\star, M_{\rm d}, q_{\rm PAH}, \gamma, U_{\rm min}, \alpha\}_j$ corresponds to a dust mass surface density:

$$\Sigma_{M_{\rm d},j} \equiv \frac{1}{D^2\Omega_j}M_{{\rm d},j}\ . \tag{5}$$

Similarly, we can compute the infrared luminosity surface density $\Sigma_{L_{\rm d},j}$ and $\Sigma_{L_{\rm PDR},j}$, the surface density of dust luminosity from regions with $U > U_{\rm PDR}$, as:

$$\Sigma_{L_{\rm d},j} \equiv \frac{1}{D^2\Omega_j}L_{{\rm d},j}, \qquad \Sigma_{L_{\rm PDR},j} \equiv \frac{1}{D^2\Omega_j}f_{{\rm PDR},j}L_{{\rm d},j}\ , \tag{6}$$

where $L_{{\rm d},j}$ is the model luminosity radiated by mass $M_{{\rm d},j}$ of dust heated by starlight characterized by $(U_{{\rm min},j}, \gamma_j, \alpha_j)$.

For each pixel j, we find the best-fit model parameters $\{U_{{\rm min},j}, \gamma_j, \alpha_j, M_{{\rm d},j}, q_{{\rm PAH},j}\}$ by minimizing χ^2, as described by AD12. After the resolved (pixel-by-pixel) modeling of the galaxy is performed, we compute a set of global quantities by adding or taking weighted means (denoted as $\langle ...\rangle$) of the quantities in each individual pixel of the map. The total dust mass $M_{\rm d}$, total dust luminosity $L_{\rm d}$, and total dust luminosity radiated by dust in regions with $U > 10^2$, $L_{\rm d,tot}$, are given by:

$$M_{\rm d} \equiv \sum_{j=1}^{N} M_{{\rm d},j}\ , \quad L_{\rm PDR} \equiv \sum_{j=1}^{N} L_{{\rm d},j}\ ,$$

$$L_{\rm PDR} \equiv \sum_{j=1}^{N} L_{{\rm PDR},j} = \sum_{j=1}^{N} L_{{\rm d},j}f_{{\rm PDR},j}\ , \tag{7}$$

where the sums extend over all the pixels j that correspond to the target galaxy (i.e., the "galaxy mask" pixels, as described in AD12). The dust-mass weighted PAH mass fraction $\langle q_{\rm PAH}\rangle$, and mean starlight intensity $\langle\overline{U}\rangle$, are given by:

$$\langle q_{\rm PAH}\rangle \equiv \frac{\sum_{j=1}^{N} q_{{\rm PAH},j}\,M_{{\rm d},j}}{\sum_{j=1}^{N} M_{{\rm d},j}}\ , \quad \langle\overline{U}\rangle \equiv \frac{\sum_{j=1}^{N}\overline{U}_j\,M_{{\rm d},j}}{\sum_{j=1}^{N} M_{{\rm d},j}}\ . \tag{8}$$

We similarly define the dust mass-weighted minimum starlight intensity

$$\langle U_{\rm min}\rangle \equiv \frac{\sum_{j=1}^{N} U_{{\rm min},j}M_{{\rm d},j}}{\sum_{j=1}^{N} M_{{\rm d},j}} \tag{9}$$

The dust-luminosity weighted value of $f_{\rm PDR}$ is:

$$\langle f_{\rm PDR}\rangle \equiv \frac{L_{\rm PDR}}{L_{\rm d}}\ . \tag{10}$$

While the average value of α is of little physical significance (the sum of two power laws is not a power law), for purposes of discussion we define a representative value

$$\langle\alpha\rangle \equiv \frac{\sum_{j=1}^{N}\gamma_j M_{{\rm d},j}U_{{\rm min},j}\alpha_j}{\sum_{j=1}^{N}\gamma_j M_{{\rm d},j}U_{{\rm min},j}}\ . \tag{11}$$

We also fit a dust model to the global photometry of each galaxy (i.e., a single-pixel dust model). Below we will compare the result of this single-pixel global model with summing over the fits to individual pixels.

5.2. *Post-Planck renormalization of DL07 dust masses and starlight intensities*

Planck Collaboration et al. (2016) fitted the DL07 dust model to all-sky maps in the *Planck* 857, 545,

Table 7. Allowed Ranges for Adjustable Parameters

Parameter	min	max		Parameter grid used
$L_\star$	0	∞		continuous fit
$M_{\rm d}$	0	∞		continuous fit
$q_{\rm PAH}$	0.00	0.10		in steps $\Delta q_{\rm PAH} = 0.001$
$f_{\rm PDR}$	0.0	$< 1.00^a$		continuous fit
$U_{\rm min}$	0.7	30	when $\lambda_{\rm max} = 160\mu$m	in steps $\Delta U_{\rm min} = 0.01^b$
	0.07	30	when $\lambda_{\rm max} = 250\mu$m	in steps $\Delta U_{\rm min} = 0.01^b$
	0.01	30	when $\lambda_{\rm max} = 350\mu$m	in steps $\Delta U_{\rm min} = 0.01^b$
	0.01	30	when $\lambda_{\rm max} \geq 500\mu$m	in steps $\Delta U_{\rm min} = 0.01^b$
α	1.0	3.0		in steps $\Delta\alpha = 0.1$
$U_{\rm max}$	10^7	10^7		not adjusted

[a] For each set of $U_{\rm min}$, $U_{\rm max}$, and α there is maximum value of $f_{\rm PDR}$ possible.

[b] The fitting procedure uses pre-calculated spectra for $U_{\rm min} \in \{0.01, 0.015, 0.02, 0.03, 0.05, 0.07, 0.1, 0.15, 0.2, 0.3, 0.4, 0.5, 0.6, 0.7, 0.8, 1.0, 1.2, 1.5, 2, 2.5, 3.0, 4.0, 5.0, 6.0, 7.0, 8.0, 10, 12, 15, 20, 25, 30\}$ interpolated onto a grid with $\Delta U_{\rm min} = 0.01$.

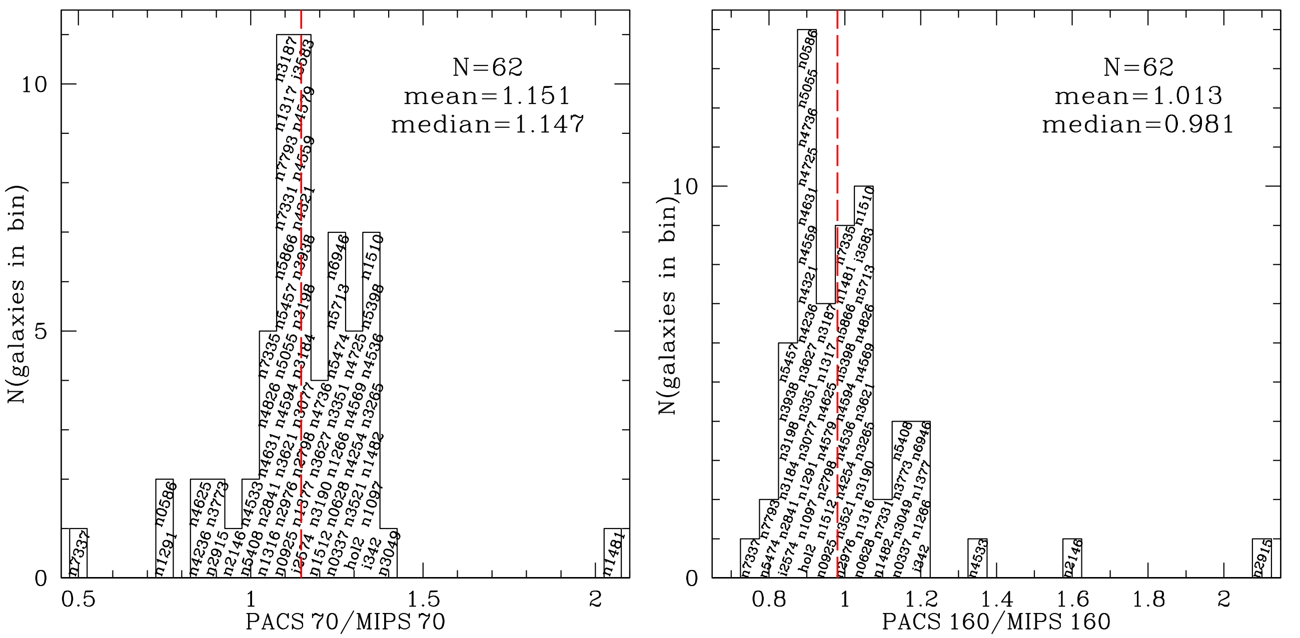

Figure 2. PACS/MIPS global photometry for the KF62 sample (see Table 1). Eight galaxies where dust was not reliably detected have been excluded (see text). Dashed lines show medians. PACS and MIPS photometry typically differs by ∼20% at 70μm, and ∼10% at 160μm, except for outliers (NGC 7337 and NGC 1481 at 70μm; NGC 2146 and NGC 2915 at 160μm). PACS70 fluxes are systematically higher than MIPS70.

353, 217, 143, and 100 GHz (350μm, 550μm, 850μm, 1.4 mm, 2.1 mm, and 3.0 mm) bands, DIRBE 100μm, 140μm, and 240μm bands, IRAS 60μm and 100μm bands, and the WISE 12μm band, to estimate the dust mass surface density for over 50 million $1.7' \times 1.7'$ pixels. About 270,000 of these pixels contain spectroscopically-confirmed SDSS quasars, which were used to estimate the correlation of quasar reddening with the reddening predicted by the DL07 dust model. It was discovered that the DL07 model tends to overpredict the reddening by a factor ∼2. The *Panchromatic Hubble Andromeda Treasury* (PHAT) study of stars in M31 (Dalcanton et al. 2015) also found that the DL07 dust model, if constrained to reproduce the observed infrared emission (Draine et al. 2014), overpredicted the reddening of stars in M31 by a factor ∼2. The SDSS quasars allow the bias factor to be estimated: Planck Collaboration et al. (2016) found that the bias appeared to depend on the value of $U_{\rm min}$:

$$\frac{E(B-V)_{\rm QSO}}{E(B-V)_{\rm DL07}} \approx 0.42+0.28U_{\rm min} \quad \text{for} \quad 0.4 \lesssim U_{\rm min} \lesssim 1.0 \,. \tag{12}$$

If the reddening $E(B-V)$ has been overestimated, it is reasonable to suppose that the dust mass/area has also been overestimated, by approximately the same factor as the reddening. Therefore, we will correct the DL07 dust mass estimates by the same empirical correction factor as for the reddening.

Because the KINGFISH sample includes some pixels with high $U_{\rm min}$, we choose to limit the *Planck*-derived correction factor for $U_{\rm min} > 1$:

$$\Sigma_{M_{\rm d},{\rm renorm},j} = C_{{\rm dust},j} \times \Sigma_{M_{\rm d},{\rm DL07},j} \quad (13)$$

$$C_{{\rm dust},j} = 0.42 + 0.28\min(U_{\rm min,j}, 1.0) \quad . \quad (14)$$

Because the dust models are required to reproduce the dust luminosity, a reduction in the estimated amount of dust implies a corresponding increase in the estimated starlight intensities. Thus we take, for pixel j:

$$\bar{U}_{{\rm renorm},j} = \frac{1}{C_{{\rm dust},j}}\bar{U}_{{\rm DL07},j} \quad (15)$$

and

$$U_{{\rm min,renorm},j} \approx \frac{1}{C_{{\rm dust},j}} U_{{\rm min,DL07},j} \quad . \quad (16)$$

All of the dust and starlight parameters ($M_{\rm d}$, $U_{\rm min}$) reported below are "renormalized" values from Eq. (13) and (16).

The above "renormalization" is required because observations indicate that the far-infrared and submm opacity of interstellar dust per unit reddening is somewhat larger than the DL07 model values.[7] We will find below (Table 9) that the global average $\langle C_{\rm dust}\rangle$ for the 62 galaxies ranges from 0.45 to 0.69, with median $\langle C_{\rm dust}\rangle = 0.62$. Thus the typical correction relative to the DL07 model is a reduction in $M_{\rm d}$ by a factor $\sim$0.62.

Because Eq. (13) has $C_{\rm dust} = 0.70$ for $U_{\rm min} \geq 1$, the estimated dust-to-gas ratio in regions with $U_{\rm min} \geq 1$ is reduced by a constant factor 0.70. This applies to the study of Sandstrom et al. (2013), which was dominated by regions with $\langle U\rangle > 1$. However, because $C_{\rm dust} =$ *constant*, the CO-to-H_2 ratios found by Sandstrom et al. (2013) are unaffected by the renormlization.

5.3. *Why both MIPS and PACS are needed*

As discussed by Aniano et al. (2011) the MIPS160 PSF cannot be convolved safely into any of the PSFs of the remaining cameras. Therefore, if we wish to include MIPS160 photometry in the dust modeling, we must "degrade" all other images into the MIPS160 PSF.

There are two reasons why we want to include MIPS160 even though PACS160 imaging is available. First, using the larger PSF increases the signal/noise ratio for the imaging, thereby allowing photometry to be extended to lower surface brightness regions. Secondly, there are significant and unexplained discrepancies between PACS160 and MIPS160 photometry. Similar discrepancies are found between PACS70 and MIPS70.

Figure 2 shows histograms of the global PACS70/ MIPS70 flux ratio (left panel), and the global PACS160/ MIPS160 flux ratio (right panel) for each of the KF62 galaxies with reliable dust detections. Each histogram shows the names of galaxies in the bin; "NGC", "DDO", "Holmberg" and "IC" are abbreviated to "n", "d", "Hol", and "i", respectively.

The PACS70 and MIPS70 bandpasses differ slightly, as do the PACS160 and MIPS160 bandpasses. However, AD12 show that for reasonable dust SEDs the slight difference in bandpasses can explain differences in reported fluxes of only $\lesssim$ 9% at 70μm, and $\sim$ 2% at 160μm, whereas much larger PACS/MIPS discrepancies are often observed.

AD12 (their Appendix F) found that even when the global photometry has PACS/MIPS $\approx$ 1, the PACS and MIPS images (with PACS convolved to the MIPS PSF) can have local surface brightnesses discrepant by factors as large as 1.5-2.0. Similar discrepancies were found when comparing PACS and MIPS imaging of M31 (Draine et al. 2014) and NGC 4449 (Calzetti et al. 2018).

Figure 2 illustrates that even after summing over the full galaxy mask, PACS70 and MIPS70 often disagree by more than a factor 1.2, and sometimes up to a factor 1.4. The median ratio is 1.17.

PACS160 and MIPS160 are generally in better agreement, but often have discrepancies larger than 10%. There are two outliers in Figure 2: NGC 2146 (PACS160/MIPS160=1.6) and NGC 2915 (PACS160/ MIPS160=2.3). The high value of PACS160/MIPS160 for NGC 2146 may be the result of sublinear response of MIPS160 on the very bright nucleus of NGC 2146. The case of NGC 2915 is unclear – the peak surface brightness is modest. Perhaps the background has been oversubtracted in the MIPS160 image, or undersubtracted in the PACS160 image.

Because it is usually unclear why PACS and MIPS disagree (the discrepancies are too large to be attributed to differences in bandpasses), we consider that both PACS and MIPS photometry should be included if we wish to estimate the dust parameters with the best accuracy available. AD12 also found that, for a given camera set, dust parameter estimates do not change significantly when using a broader PSF, therefore modeling at MIPS160 PSF does not significantly alter the dust parameter estimates. We consider our "gold standard" (i.e., the PSF and camera combination that gives the most accurate dust parameter estimates) to be resolved (i.e., multipixel) modeling done using the MIPS160 PSF, using photometry from all of the IRAC, MIPS, PACS, and SPIRE cameras.

[7] The empirical finding that $C_{\rm dust}$ depends on $U_{\rm min}$ suggests that the dust opacity may decline less rapidly with increasing λ than assumed by DL07.

6. RESULTS

For each galaxy in the KF62 sample, Table 9 presents the global dust parameters estimated for the "gold standard" modeling, including information characterizing the intensity of the starlight heating the dust in each galaxy. The modeling was done at MIPS160 PSF, using all the cameras available; we also give results of modeling at S250 resolution.

The given quantities are obtained by summing or averaging over the resolved maps using Equations (7-10). The dust masses listed in Table 9 we obtained using the DL07 model, but then "renormalized" following Equation (13). The renormalization factor $C_{\rm d}$ depends on $U_{\rm min}$, and therefore varies from pixel to pixel. The overall renormalization factor

$$\langle C_{\rm dust}\rangle \equiv \frac{\sum_{j=1}^{N} \Sigma_{{\rm Md,renorm},j}}{\sum_{j=1}^{N} \Sigma_{{\rm Md,DL07},j}} = \frac{\sum_{j=1}^{N} C_{{\rm dust},j}\Sigma_{{\rm Md,DL07},j}}{\sum_{j=1}^{N} \Sigma_{{\rm Md,DL07},j}} \quad (17)$$

for each galaxy is given in Table 9, for both M160 and S250 resolution. Henceforth, $M_{\rm d}$, $U_{\rm min}$, and $\overline{U}$ will refer to the renormalized values of these quantities [see Eq. 13-16].

6.1. *One Example: NGC 5457 = M 101*

To illustrate the quality of the data and the modeling results for the KINGFISH galaxies, we choose the large, nearly face-on spiral NGC 5457 (M 101) as an example. As for all our galaxies, the dust mass, PAH abundance, and starlight heating parameters are adjusted separately for each pixel.

The parameter α characterizes the distribution of starlight intensities heating dust within a pixel (see Eq. 1). Figure 3 shows maps of the best-fit α values for the M160 and S250 resolution modeling. At M160 resolution, α is azimuthally coherent but has a notable radial gradient, with $\alpha \approx 1.7$ in the center, and $\alpha \approx 2.3$ beyond galactocentric radius $\sim$6 kpc. While the variation in best-fit α is apparent, these values are all close to $\alpha = 2$, the case where there is equal power per unit $\log U$. At S250 resolution, the signal-to-noise ratios are lower, and the S350, S500, and M160 cameras are not used; the α map for the S250 resolution modeling shows more pixel-scale variations, but with a radial trend similar to the M160 resolution modeling.

In general, the DL07 model successfully reproduces the resolved SEDs in M 101. Figure 4 compares the model 500μm surface brightness with observations. The upper panel shows modeling at M160 resolution (the observed SPIRE500 intensity is used as a model constraint). The DL07 model is generally within $\pm$10% of the observed SPIRE500 intensity, except at the outer edges of the mask where the signal/noise is low. The model appears to fall short by $\sim$10% in the outer regions (galactocentric radius $\sim$15 kpc=0.13°), where the metallicity has dropped to $12 + \log_{10}({\rm O/H}) \approx 8.25$ (Li et al. 2013). This could indicate that the frequency dependence of the dust opacity becomes less steep as the metallicity drops – consistent with the SED of the SMC (Israel et al. 2010; Bot et al. 2010; Planck Collaboration et al. 2011; Draine & Hensley 2012), and with evidence for a submm excess in galaxies with metallicities $12 + \log_{10}({\rm O/H}) \leq 8.3$ (Rémy-Ruyer et al. 2013).

The lower panel of Figure 4 compares modeling at S250 resolution (no data longward of 250μm used to constrain the model) with the SPIRE500 observations. In the bright spiral arms, the 500μm intensity is overpredicted by $\sim$25%. Once again we see a radial gradient: the model overpredicts SPIRE500 in the central regions, and underpredicts SPIRE500 at $R \gtrsim 8\,{\rm kpc} = 0.07°$. In the outer regions the fit is poorer, presumably due to the low signal/noise ratio at S250 resolution.

Figure 5 shows maps of dust and starlight heating parameters for M 101. There are 2 sets of figures; the first set (rows 1 and 2) corresponds to modeling done at M160 resolution, using data from all (IRAC, MIPS, PACS, and SPIRE) cameras, i.e., "gold standard" modeling, and the second (rows 3 and 4) to modeling done at S250 resolution, using IRAC, MIPS24, PACS, and SPIRE250 cameras. This latter modeling is able to resolve smaller scale structures in the galaxies, but is overall less reliable, particularly in the outer regions where the surface brightness is lower and dust is cooler.

Because of the proximity of M 101 ($D = 6.7$ Mpc), the spiral structure is visible even at M160 resolution. At M160 resolution 38.8 arcsec FWHM), the dust luminosity/area ranges from the surface brightness $\Sigma_{Ld,{\rm min}} = 0.67 L_\odot\,{\rm pc}^{-2}$ defining the boundary of the galaxy mask to a peak $\Sigma_{Ld} = 10^{2.5} L_\odot\,{\rm pc}^{-2} \sim 8.5$ kpc ESE of the center, at the position of the giant H II region NGC 5461 (see, e.g., Esteban et al. 2009).

At S250 resolution the peak at NGC 5461 has a dust/luminosity/area $\Sigma_{Ld} = 10^{3.2} L_\odot\,{\rm pc}^{-2}$ [corresponding to a dust luminosity $L_{\rm d} = 6 \times 10^7 L_\odot$ in a single $195 \times 195\,{\rm pc}^2$ S250 map pixel]. Thus at S250 resolution, we are able to measure the IR emission from the dust over a dynamic range of $\sim$2000 in Σ_{Ld}.

Maps of dust surface density Σ_{Md} are also shown for both the M160 and S250 modeling. At both M160 and S250 resolution Σ_{Md} has a peak at the extranuclear luminosity peak. At S250 resolution we estimate a peak dust surface density $5 \times 10^5 M_\odot\,{\rm kpc}^{-2}$, corresponding to $M_{\rm d} = 2 \times 10^4 M_\odot$ of dust in a single S250 map pixel.

Maps of the starlight modeling parameter $U_{\rm min,DL07}$ are also shown at both M160 and S250 resolution. In M101, $U_{\rm min,DL07}$ ranges from values as high as 30 (the largest value permitted by our modeling) to values as low as $\sim$ 0.07 in the outer parts of the galaxy. The highest values of $U_{\rm min} = 30$ arise in the S250 modeling, with high values of $U_{\rm min}$ appearing in a fraction of pixels in low surface brightness regions to the east of the center. The high $U_{\rm min}$ values found in these regions using S250 resolution data are probably unphysical, arising as

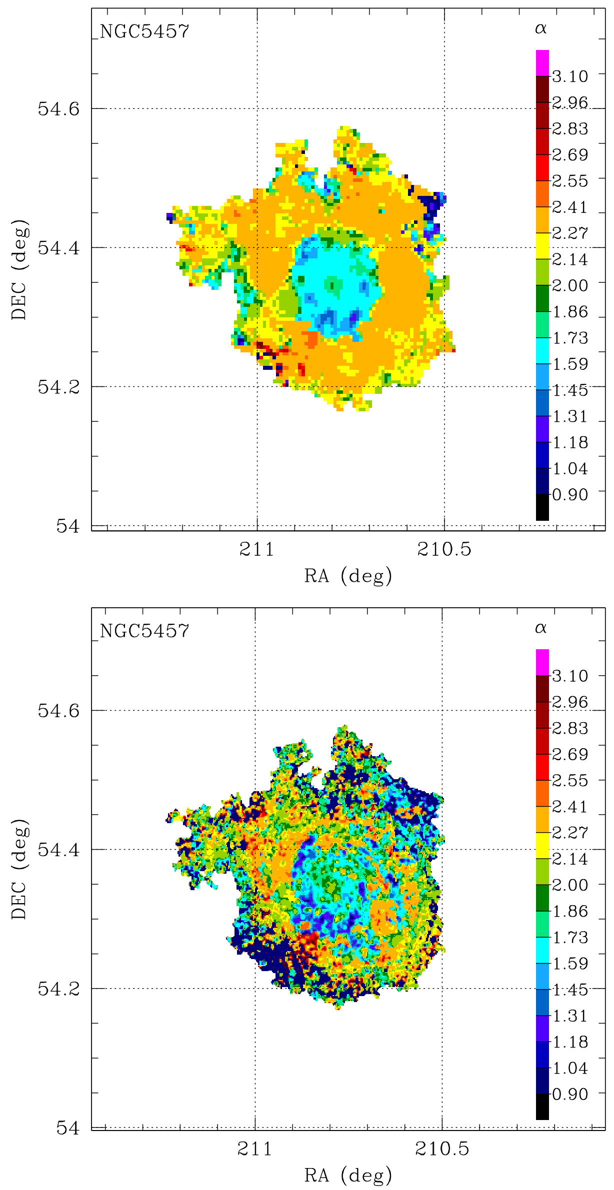

Figure 3. Starlight heating parameter α for NGC 5457 = M101, for modeling at M160 resolution (top) and at S250 resolution (bottom), for the "galaxy mask" defined by $\Sigma_{Ld} > \Sigma_{Ld,\rm min} = 0.67 L_\odot\,{\rm pc}^{-2}$. At M160 resolution, where all cameras are used to constrain the model, α is azimuthally coherent but with a radial gradient: $\alpha \approx 1.7$ in the center, and $\alpha \approx 2.3$ in the outer regions. The S250 map is noisier, because not all of the cameras can be used, and the signal-to-noise ratio of the bands that can be used is reduced.

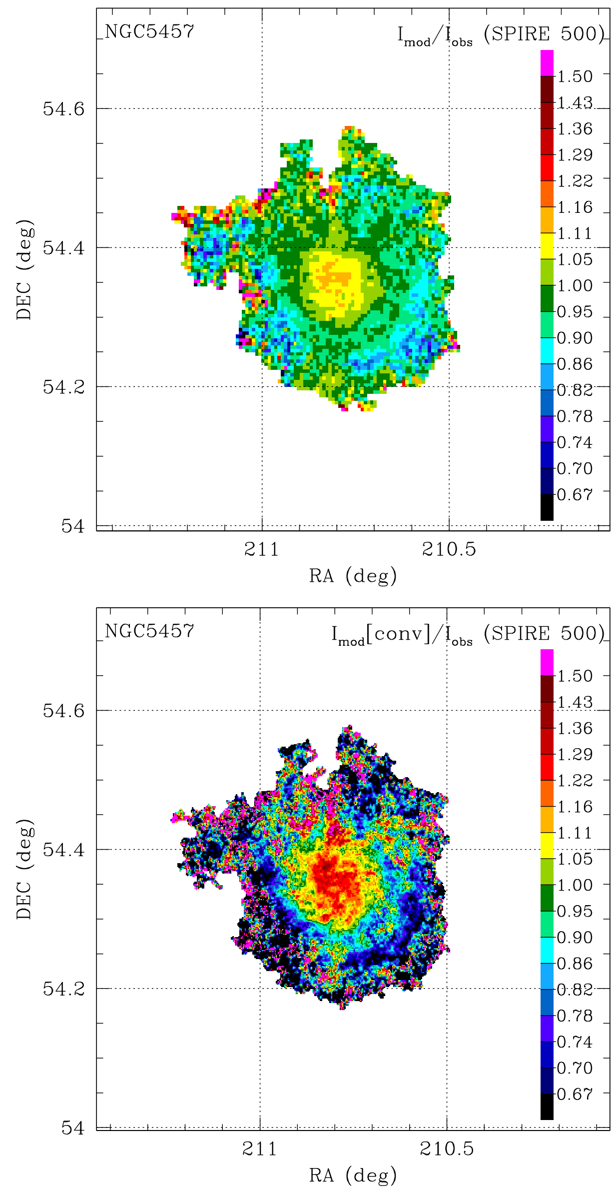

Figure 4. $I_\nu^{\rm model}/I_\nu^{\rm obs}$ for NGC 5457, for modeling at M160 resolution (top) and S250 resolution (bottom). At M160 resolution, the model reproduces the SPIRE500 observations to within $\sim$15%, with a clear radial gradient in model/observation, suggesting a systematic change in the dust opacity with changing metallicity (see text). At S250 resolution, no data longward of 250μm are used to constrain the model; the predicted 500μm intensity (after convolving to the SPIRE500 PSF) agrees with observations to within $\sim$25%. A radial gradient is again seen.

the result of low S/N data: an upward fluctuation in PACS70 (or a downward fluctuation in SPIRE250) can drive the fitting to a high $U_{\rm min}$ value. Within $\sim 5\,$kpc of the center, with higher surface brightnesses, we generally find $0.5 \lesssim U_{\rm min} \lesssim 4$. And in the M160 modeling, we do not obtain very high values of $U_{\rm min}$ even in the low surface brightness outer regions.

Maps of $q_{\rm PAH}$ are also shown at both M160 and S250 resolution. The modeling finds a very high value of $q_{\rm PAH}$ along the SSE edge of the galaxy; this is seen in both the M160 and S250 modeling of an extended region approx-

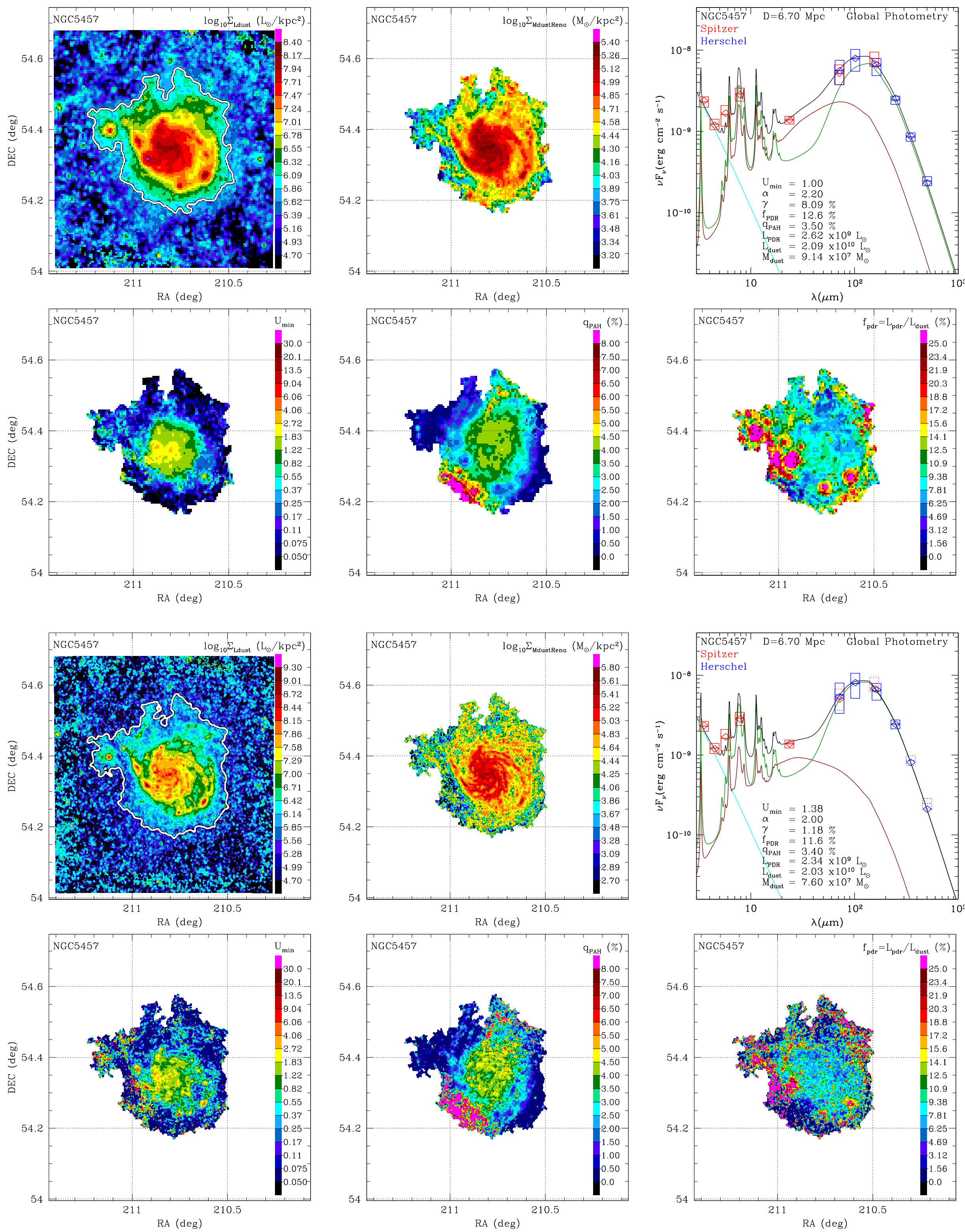

Figure 5. NGC5457 = M101: model results at M160 PSF (rows 1 and 2) and at S250 PSF (rows 3 and 4). Dust luminosity per area Σ_{Ld} (column 1, rows 1 and 3) is shown for entire field, with adopted galaxy mask boundary in white. Dust mass per area Σ_{Md} (column 2, rows 1 and 3) is after renormalization (see text). $U_{\rm min,DL07}$, $q_{\rm PAH}$ and $f_{\rm PDR}$ are shown in rows 2 and 4. The global SED (column 3, rows 1 and 3) is shown for single-pixel modeling, with contributions from dust heated by $U_{\rm min}$ (green), dust heated by $U > U_{\rm min}$ (red) and starlight (cyan); values of $U_{\rm min}$ and $M_{\rm d}$ in the figure label are for the DL07 model before renormalization. *Herschel* (blue rectangles) and *Spitzer* (red rectangles) photometry is shown. Diamonds show the band-convolved flux for the model. Horizontal extent of rectangles and diamonds is an arbitrary ±10% wavelength range. Vertical extent of photometry rectangles is $\pm 1\sigma$.

imately 12 kpc SSE of the center. The high estimates for $q_{\rm PAH}$ could arise from errors in the IRAC 5.6 and 8μm photometry, probably due to errors in background subtraction.

Maps of $f_{\rm PDR}$ – the fraction of the dust luminosity that is contributed by dust heated by starlight with $U > 100$ – are shown at both M160 and S250 resolution. High values of $f_{\rm PDR}$ are seen at many of the positions where Σ_{Ld} peaks, which is consistent with the idea that these are regions with active star formation, with some fraction of the dust exposed to intense radiation fields in or near OB associations. However, we also see high $f_{\rm PDR}$ values in some of the lowest surface brightness regions near the edge of the galaxy mask – this is presumably an indication that photometric errors and errors in background subtraction are leading to overestimation of 24 or 70μm emission relative to the total dust luminosity. Thus our derived values of $f_{\rm PDR}$ appear to be unreliable in the lowest surface brightness regions.

We also show the global SED for M101, extracted from the galaxy mask. In the upper right panel, the rectangular symbols show the measured fluxes $\pm 1\sigma$ for the 7 Spitzer cameras and the 6 Herschel cameras. At 70μm and 160μm both red and blue rectangles are shown, with the MIPS and PACS photometry. Also shown is a *single-pixel* DL07 model, where the DL07 model is fitted to the global photometry. The diamonds show the model fluxes for each of the instrumental bandpasses. In the case of M101, the model (with 6 adjustable parameters – $L_\star, M_{\rm d}, q_{\rm PAH}, U_{\rm min}, \gamma, \alpha$) is consistent with the photometry at 11 independent wavelengths (3.6μm to 500μm). In row 3 column 3 we show a single-pixel DL07 model fitted to only the photometry that is used for the S250 modeling (i.e., MIPS70, MIPS160, SPIRE350, or SPIRE500 are *not* used when adjusting the model parameters). The dashed rectangles show these unused measurements; we see that for M 101 the single-pixel model does quite well at *predicting* the fluxes at 350 and 500μm, with only a 1σ underprediction even at 500μm. The single-pixel global fit parameters are given in the SED plots.

Table 8 compares total dust mass estimates for M101. Column 2 reports the dust mass estimated from the DL07 model at either M160 or S250 resolution, after summing the dust model over the galaxy mask. Because we opted to use the same $\Sigma_{Ld,{\rm min}}$ for the S250 and M160 modeling, the galaxy masks for the two cases are essentially the same. Column 3 reports the result of fitting a DL07 model to the global photometry – this is referred to as "single pixel" modeling. In columns 4 and 5 we show the multipixel or single pixel dust masses after renormalizing following Equation 13.

Multipixel vs. single-pixel modeling is of course expected to produce different estimates because the models are nonlinear. One notes in Table 8 that the discrepancies between the multipixel and single pixel mass estimators are reduced when going from the original DL07 model to the renormalized model. It is not clear why this is the case, but this is a welcome result.

Table 8. Dust mass estimates for NGC 5457=M 101

PSF	$M_{\rm d}/10^7 M_\odot$				
	DL07		renorm. DL07		multipix
	multipixel	single pixel	multipixel	single pixel	$\langle C_{\rm dust}\rangle$
M160	12.7 ± 0.5	9.14 ± 0.32	6.97 ± 0.20	6.40 ± 0.89	0.549
S250	12.1 ± 2.9	7.60 ± 0.10	6.88 ± 1.34	5.32 ± 0.28	0.569

6.2. *Full KINGFISH Sample*

Dust is detected reliably for every galaxy in the KF62 sample. Selected images for each of these galaxies are given in Appendix A (Figures 17.1-17.62, following the scheme used for M 101 in Fig. 5. This is only a fraction of the maps and images that are available online – see Appendix C for a description of the data set.

The "galaxy mask" for each galaxy is shown for both the M160 PSF and the S250 PSF. As for M101, we have opted to use the same $\Sigma_{Ld,{\rm min}}$ for both the M160 and S250 modeling, hence the M160 and S250 $\Sigma_{Ld,{\rm min}}$-based galaxy masks are nearly identical for each galaxy, except for the 8 where dust emission is so weak that we treat them as nondetections (see Appendix B). The flux densities F_ν measured by *Spitzer* and *Herschel* within the M160 and S250 galaxy mask for each galaxy have been given above in Tables 5 and 6. The model-derived parameters for the dust and starlight are given in Table 9. α is not included in Table 9 because there is no natural way to define a "mean" α for multipixel modeling. The uncertainties listed for the parameters are based on repeating the fitting procedure with the "observed" fluxes obtained by Monte-Carlo sampling from Gaussian distributions with means and widths given by the original observed values and uncertainty estimates (see discussion in Appendix E of AD12). Systematic errors associated with the DL07 model itself have not been estimated.

Figures 17.1-17.62 have twelve panels in all, with the top six panels showing results of modeling with the M160 PSF, and the lower six panels repeating this for the S250 PSF. For each PSF, the top row shows maps of the dust luminosity surface density $\Sigma_{L_{\rm d}}$ (upper left) and modeled dust surface density $\Sigma_{M_{\rm d}}$ (upper center), and the model SED (upper right). The lower row shows maps of the starlight intensity parameter $U_{\rm min}$ (left), the PAH abundance parameter $q_{\rm PAH}$ (center), and the PDR fraction $f_{\rm PDR}$ (right), all restricted to the "galaxy mask".

In the SED plot, the observed global photometry is represented by rectangular boxes [*Spitzer* (IRAC and MIPS) in red; *Herschel* (PACS and SPIRE) in blue]. The vertical extent of each box shows the $\pm 1\sigma$ uncertainty in the photometry for each band. The black line is the total DL07 model spectrum, and its different components are represented by three colors. The cyan line is the stellar contribution, the dark red line is the emission from dust heated by the power-law U distribution, and the dark green line is emission from dust heated by $U = U_{\rm min}$. The DL07 model used in this SED plot is a single-pixel model, which tries to reproduce the global photometry treating the entire galaxy as a single pixel. These "single pixel" models generally do a good job at reproducing the global photometry. Multipixel models, where the photometry in every pixel is fit independently, have many more adjustable parameters, and naturally do an even better job of reproducing the global photometry after summing over all the pixels in the galaxy mask. It is reasonable to presume that models that do a better job of reproducing the photometry will also be preferred for dust mass estimation.

The dust mass surface densities and dust luminosities per unit area range over three orders of magnitude in our brightest galaxies. Figures 17.1-17.62 illustrate that the DL07 model does a satisfactory job of fitting the SEDs. Although each pixel is modeled independently of its neighbors, it is noteworthy that the dust parameters are smoothly varying over the confines of the galaxy, except for the low surface brightness outer regions at S250 resolution, where the S/N in individual pixels may become low enough that certain dust and starlight parameters, such as Σ_{Md} and $U_{\rm min}$, become somewhat noisy.

6.3. *Special Cases*

6.3.1. *NGC 1404*

The E1 galaxy NGC 1404 is faint at infrared wavelengths, and there is a foreground star $\sim 180''$ to the SSE. However, NGC 1404 is unambiguously detected in IRAC bands 1-4, and by MIPS24. At $\lambda \geq 70\mu$m there appears to be excess emission at the position of NGC 1404, but the surface brightness is low and the possibility that the emission is from a foreground or background source cannot be excluded (Dale et al. 2012). Using the procedure described in Appendix B, we find a 3σ upper bound $M_{\rm dust} < 2.0 \times 10^6 M_\odot$ for NGC 1404.

NGC 1404 has an estimated stellar mass $M_\star \approx 8 \times 10^{10} M_\odot$, and evolved stars are probably injecting dust at a rate $\dot{M}_{\rm dust} \approx 0.005 \times M_\star/10^{10}\,{\rm yr} = 0.04 M_\odot\,{\rm yr}^{-1}$.[8] Thus the observed dust mass upper limit would be consistent with a dust lifetime $M_{\rm d}/\dot{M}_{\rm dust} \lesssim 5 \times 10^7\,{\rm yr}$. If the ISM in NGC 1404 has a temperature $T \approx 10^7\,{\rm K}$, silicate or carbonaceous dust grains would be eroded by thermal sputtering at a rate $da/dt \approx -1 \times 10^{-10}\,{\rm cm\,yr^{-1}}(n_{\rm H}/\,{\rm cm^{-3}})$ (Draine & Salpeter 1979), for a grain lifetime $a/|da/dt| = 10^7 (a/0.1\mu{\rm m})(0.01\,{\rm cm^{-3}}/n_{\rm H})\,{\rm yr}$. The dust mass upper limit would thus be consistent with erosion of $a \approx 0.1\mu$m grains by sputtering in a $T \approx 10^7\,{\rm K}$ ISM with $n_{\rm H} \gtrsim 0.002\,{\rm cm^{-3}}$.

[8] A rough estimate, assuming $\sim 1 M_\odot$ stars each lose $\sim 0.5 M_\odot$ of envelope before becoming white dwarfs, and that $\sim 1\%$ of the envelope mass consists of dust.

6.3.2. *NGC 1377*

NGC 1377 has a compact dusty core, with an extremely high far-infrared surface brightness. The infrared spectrum (Roussel et al. 2006) shows that it is optically thick at $\lambda \lesssim 20\mu$m. Weak PAH emission is detected, but because of the uncertain infrared extinction it is not possible to reliably estimate the PAH abundance parameter $q_{\rm PAH}$. The dust mass estimates should also be regarded as uncertain because of the unusual nature of the interstellar medium in this galaxy.

6.4. *Gold-Standard DL07 fit results for KINGFISH galaxies*

Figure 6 shows the dust parameter distributions for the 61 KINGFISH galaxies plus 9 "extras". The dust parameters shown are the result of the "gold standard" modeling – multipixel modeling for each galaxy using the M160 PSF and data from all cameras.

The first row shows the distributions of $M_{\rm d}$ (left column) and $L_{\rm d}$ (right column) for the KF62 galaxies. The second row shows the distributions of $\langle U \rangle$ (left column) and $q_{\rm PAH}$ right column), and the bottom row shows the distributions of $\langle f_{\rm PDR} \rangle$ (left column) and $\langle \alpha \rangle$ (right column). In these histograms, the dust masses $M_{\rm d}$ and $\langle U \rangle$ are renormalized, as discussed in Section 5.2.

Figure 6 illustrates the large region in the model parameter space spanned by the KINGFISH sample, allowing us to probe the dust properties in a variety of ISM conditions. The total dust mass and dust luminosity found in the galaxies spans almost 4 decades: $10^{4.5} \leq M_{\rm d}/M_\odot \leq 10^{8.0}$ and $10^{7.5} \leq L_{\rm d}/L_\odot \leq 10^{11.1}$, from the blue dwarf NGC 2915 ($L_{\rm d} = 3.3 \times 10^7 L_\odot$) to the luminous starburst galaxy NGC2146 ($L_{\rm d} = 1.4 \times 10^{11} L_\odot$).

The mean value of the starlight heating parameter $U_{\rm min}$ also presents wide variations across the galaxy sample. $\langle U_{\rm min} \rangle$ spans the range $0.1 \leq \langle U_{\rm min} \rangle \leq 8.5$ (these values of $U_{\rm min}$ are for the DL07 model without renormalization). The PAH mass fraction $q_{\rm PAH}$ also shows wide variation, from 0.005 to 0.045, with median $q_{\rm PAH} = 0.027$. The mean fraction of the dust luminosity coming from dust heated by high-intensity radiation fields, $\langle f_{\rm PDR} \rangle$, typically ranges from 0.05 to 0.20.

There are 4 KINGFISH galaxies where the fitted DL07 dust models have very high values of $\langle f_{\rm PDR} \rangle > 0.30$: NGC 1316 = Fornax A (SAB0), NGC 3049 (SBab), NGC 3265 (E), NGC 5408 (IBm), and the "extra" galaxy NGC 1510 (SA0). NGC 1316 = Fornax A has a central AGN/LINER spectrum, and NGC 3265 has an emission-line nuclear region (Dellenbusch et al. 2008), NGC 1510 hosts a strong central starburst, and NGC 3049 and NGC 5408 are often classified as starburst galaxies. Thus the high $\langle f_{\rm PDR} \rangle$ values for these galaxies may be indicative of concentrated star formation or nuclear activity.

Finally, the mean power-law exponent $\langle \alpha \rangle$ spans $1.5 \leq \langle \alpha \rangle \leq 2.5$. Allowing α to vary does improve the quality

Table 9. Dust Model Parameters for S250 and M160 Galaxy Masks

Galaxy	mask	$M_{\rm dust}(10^6 M_\odot)^a$	$q_{\rm PAH}(\%)$	$\langle U_{\rm min}\rangle^a$	$\langle \bar{U}\rangle^a$	$f_{\rm PDR}(\%)$	$\langle C_{\rm dust}\rangle$	$L_{\rm dust}(10^9 L_\odot)$
Hol2	S250	0.12 ± 0.05	0.95 ± 0.67	2.4 ± 4.6	3.1 ± 3.7	15.3 ± 4.1	0.500	0.061 ± 0.009
”	M160	0.134 ± 0.033	0.68 ± 0.34	1.0 ± 1.6	2.7 ± 0.9	18.1 ± 3.4	0.491	0.058 ± 0.006
IC342	S250	$41. \pm 8.$	4.4 ± 0.8	1.9 ± 1.3	2.5 ± 1.2	12.9 ± 2.4	0.614	16.5 ± 2.3
”	M160	$35. \pm 5.$	4.25 ± 0.26	2.2 ± 0.6	2.7 ± 0.5	12.8 ± 3.7	0.640	16.0 ± 0.8
IC2574	S250	1.08 ± 0.23	0.48 ± 0.07	0.56 ± 0.57	0.95 ± 0.50	11.8 ± 3.7	0.469	0.169 ± 0.025
”	M160	1.17 ± 0.34	0.44 ± 0.27	0.22 ± 0.21	0.85 ± 0.45	12.5 ± 1.0	0.452	0.163 ± 0.015
NGC0337	S250	10.6 ± 2.2	2.05 ± 0.25	6.3 ± 1.8	7.0 ± 1.9	11.0 ± 2.3	0.685	12.1 ± 1.3
”	M160	12.2 ± 1.0	2.4 ± 0.6	5.0 ± 0.6	5.4 ± 0.6	13.6 ± 0.6	0.678	10.8 ± 0.6
NGC0628	S250	20.5 ± 1.1	3.5 ± 0.7	1.96 ± 0.44	2.16 ± 0.34	11.5 ± 4.2	0.613	7.3 ± 1.0
”	M160	18.7 ± 1.0	3.6 ± 0.7	2.16 ± 0.21	2.30 ± 0.27	11.4 ± 2.1	0.622	7.08 ± 0.18
NGC0925	S250	$16. \pm 5.$	2.59 ± 0.36	1.2 ± 1.3	1.5 ± 1.3	8.5 ± 2.5	0.525	3.88 ± 0.36
”	M160	17.1 ± 2.7	2.65 ± 0.47	0.56 ± 0.60	1.32 ± 0.37	9.3 ± 1.2	0.481	3.721 ± 0.027
NGC1097	S250	$93. \pm 31.$	3.7 ± 0.9	2.4 ± 1.3	2.9 ± 1.2	$16. \pm 5.$	0.549	$44. \pm 7.$
”	M160	$65. \pm 7.$	3.2 ± 0.9	3.4 ± 1.0	4.0 ± 0.9	16.6 ± 3.4	0.622	42.6 ± 2.5
NGC1266	S250	13.2 ± 1.9	0.60 ± 0.16	$13. \pm 5.$	$13. \pm 5.$	13.6 ± 3.9	0.576	27.5 ± 4.7
”	M160	9.6 ± 1.0	0.61 ± 0.44	$17. \pm 6.$	15.7 ± 2.6	$15. \pm 5.$	0.635	24.7 ± 2.3
NGC1291	S250	$25. \pm 7.$	2.6 ± 0.8	0.54 ± 0.49	0.64 ± 0.57	8.4 ± 0.6	0.470	2.7 ± 0.7
”	M160	16.0 ± 4.4	2.4 ± 1.2	0.97 ± 0.27	1.04 ± 0.25	7.6 ± 3.3	0.516	2.72 ± 0.09
NGC1316	S250	12.0 ± 2.9	1.8 ± 1.0	2.8 ± 1.8	3.2 ± 1.8	10.2 ± 2.7	0.612	6.22 ± 0.45
”	M160	8.7 ± 1.3	1.9 ± 1.3	3.8 ± 0.7	4.2 ± 0.6	10.5 ± 3.1	0.660	5.90 ± 0.31
NGC1377	S250	2.5 ± 0.6	0.68 ± 0.15	$17. \pm 7.$	$34. \pm 15.$	56.7 ± 3.7	0.580	13.8 ± 1.3
”	M160	1.48 ± 0.22	0.73 ± 0.80	25.1 ± 3.8	$53. \pm 8.$	55.9 ± 1.3	0.673	12.81 ± 0.13
NGC1482	S250	20.4 ± 2.0	3.05 ± 0.38	13.8 ± 2.2	14.7 ± 2.4	12.2 ± 1.1	0.663	$49. \pm 6.$
”	M160	16.6 ± 2.1	3.3 ± 0.5	15.5 ± 3.4	16.9 ± 3.4	11.7 ± 3.5	0.686	46.4 ± 4.8
NGC1512	S250	10.1 ± 1.3	3.4 ± 0.7	1.63 ± 0.44	1.80 ± 0.41	7.5 ± 1.5	0.584	2.99 ± 0.32
”	M160	12.4 ± 1.2	3.3 ± 0.5	1.48 ± 0.35	1.50 ± 0.26	7.5 ± 1.8	0.553	3.06 ± 0.16
NGC2146	S250	$53. \pm 13.$	4.1 ± 0.7	14.6 ± 4.5	15.3 ± 3.5	12.6 ± 3.1	0.665	$135. \pm 12.$
”	M160	40.2 ± 2.2	4.2 ± 0.7	17.9 ± 4.4	20.6 ± 1.7	11.8 ± 3.1	0.692	$137. \pm 7.$
NGC2798	S250	15.8 ± 2.1	1.91 ± 0.41	14.7 ± 3.4	13.9 ± 2.8	14.5 ± 2.1	0.604	36.0 ± 3.9
”	M160	11.4 ± 0.6	2.19 ± 0.28	16.9 ± 2.1	17.99 ± 0.44	13.6 ± 2.0	0.683	33.4 ± 1.2
NGC2841	S250	$68. \pm 9.$	3.4 ± 1.1	0.84 ± 0.19	0.92 ± 0.15	6.5 ± 3.2	0.540	10.37 ± 0.36
”	M160	53.0 ± 4.0	3.40 ± 0.48	1.11 ± 0.11	1.15 ± 0.11	6.6 ± 2.3	0.584	10.03 ± 0.20
NGC2915	S250	0.052 ± 0.029	1.3 ± 0.6	3.7 ± 2.0	4.5 ± 1.7	10.1 ± 1.9	0.588	0.0377 ± 0.0046
”	M160	0.031 ± 0.010	1.4 ± 0.7	6.0 ± 2.2	6.6 ± 1.9	11.1 ± 2.0	0.676	0.0332 ± 0.0023
NGC2976	S250	1.76 ± 0.31	2.93 ± 0.20	2.6 ± 0.6	2.8 ± 0.5	10.6 ± 1.2	0.611	0.800 ± 0.034
”	M160	1.77 ± 0.11	3.2 ± 1.0	1.9 ± 0.5	2.67 ± 0.31	11.4 ± 2.2	0.661	0.778 ± 0.049
NGC3049	S250	6.6 ± 2.5	1.81 ± 0.21	2.1 ± 4.5	3.6 ± 4.7	27.4 ± 3.0	0.542	3.93 ± 0.32
”	M160	9.5 ± 0.8	2.1 ± 0.6	0.28 ± 0.52	2.09 ± 0.19	33.6 ± 1.5	0.472	3.24 ± 0.11
NGC3077	S250	1.83 ± 0.33	3.5 ± 0.6	2.2 ± 1.1	2.6 ± 0.9	13.9 ± 1.4	0.506	0.79 ± 0.11
”	M160	1.51 ± 0.15	3.1 ± 0.8	2.69 ± 0.11	3.03 ± 0.33	14.1 ± 2.1	0.529	0.754 ± 0.020
NGC3184	S250	35.7 ± 4.1	3.8 ± 0.8	1.45 ± 0.28	1.58 ± 0.14	9.8 ± 1.5	0.581	9.4 ± 0.8
”	M160	30.2 ± 2.7	3.8 ± 0.8	1.72 ± 0.21	1.82 ± 0.24	9.6 ± 3.4	0.612	9.08 ± 0.33
NGC3190	S250	21.6 ± 3.8	3.00 ± 0.26	1.77 ± 0.48	1.87 ± 0.31	4.0 ± 0.5	0.588	6.64 ± 0.24
”	M160	14.8 ± 2.0	2.8 ± 0.5	2.4 ± 0.6	2.55 ± 0.48	3.8 ± 1.3	0.681	6.19 ± 0.33
NGC3198	S250	26.8 ± 4.0	2.90 ± 0.38	1.4 ± 0.6	1.82 ± 0.47	14.6 ± 1.8	0.581	8.02 ± 0.14
”	M160	28.4 ± 2.8	3.1 ± 0.8	1.49 ± 0.31	1.65 ± 0.39	15.0 ± 3.0	0.555	7.71 ± 0.28
NGC3265	S250	2.4 ± 1.1	1.73 ± 0.47	5.2 ± 9.3	7.1 ± 9.7	$27. \pm 7.$	0.542	2.74 ± 0.10
”	M160	2.0 ± 0.9	2.30 ± 0.35	4.6 ± 2.4	7.6 ± 2.7	30.1 ± 3.3	0.576	2.49 ± 0.17
NGC3351	S250	$24. \pm 6.$	3.9 ± 1.5	1.4 ± 0.6	1.9 ± 0.5	$17. \pm 6.$	0.538	7.4 ± 0.9
”	M160	14.9 ± 1.0	3.2 ± 0.6	2.3 ± 0.6	2.85 ± 0.45	17.3 ± 3.8	0.623	6.99 ± 0.45
NGC3521	S250	$89. \pm 12.$	4.16 ± 0.35	2.21 ± 0.29	2.34 ± 0.40	8.9 ± 2.0	0.586	34.5 ± 0.7
”	M160	$69. \pm 8.$	4.17 ± 0.16	2.8 ± 0.6	2.96 ± 0.39	8.7 ± 4.4	0.648	33.7 ± 1.3
NGC3621	S250	$20. \pm 6.$	4.18 ± 0.38	2.0 ± 0.8	2.2 ± 0.6	10.8 ± 1.1	0.569	7.39 ± 0.41
”	M160	19.5 ± 3.3	4.8 ± 0.7	2.5 ± 0.7	2.23 ± 0.38	10.7 ± 2.8	0.567	7.28 ± 0.25
NGC3627	S250	$38. \pm 7.$	3.3 ± 0.7	3.9 ± 1.8	4.3 ± 1.9	12.0 ± 1.5	0.645	27.0 ± 2.7
”	M160	30.1 ± 1.5	3.23 ± 0.32	4.85 ± 0.47	5.43 ± 0.40	11.7 ± 1.9	0.691	26.9 ± 0.8
NGC3773	S250	1.12 ± 0.49	1.27 ± 0.35	2.6 ± 4.1	3.4 ± 4.0	21.3 ± 4.3	0.519	0.63 ± 0.10
”	M160	0.62 ± 0.07	1.90 ± 0.43	4.0 ± 1.5	5.5 ± 1.0	23.8 ± 3.6	0.631	0.563 ± 0.023
NGC3938	S250	$52. \pm 14.$	3.71 ± 0.35	1.8 ± 0.7	2.0 ± 0.8	9.7 ± 3.4	0.572	16.9 ± 1.4
”	M160	41.5 ± 2.5	3.7 ± 0.7	2.26 ± 0.30	2.41 ± 0.31	9.3 ± 2.2	0.627	16.5 ± 1.0
NGC4236	S250	2.12 ± 0.45	0.94 ± 0.32	0.64 ± 0.76	1.1 ± 0.7	14.4 ± 4.3	0.494	0.384 ± 0.043
”	M160	2.6 ± 1.4	0.86 ± 0.39	0.23 ± 0.10	0.85 ± 0.29	15.5 ± 1.7	0.449	0.367 ± 0.038

a Renormalized as described in §5.2.

Table 9. Dust Model Parameters, contd.

Galaxy	mask	$M_{\rm dust}(10^6 M_\odot)^a$	$q_{\rm PAH}(\%)$	$\langle U_{\rm min}\rangle^a$	$\langle \bar{U}\rangle^a$	$f_{\rm PDR}(\%)$	$\langle C_{\rm dust}\rangle$	$L_{\rm dust}(10^9 L_\odot)$
NGC4254	S250	$66. \pm 16.$	4.3 ± 1.1	3.4 ± 1.0	3.6 ± 1.1	11.8 ± 3.0	0.631	39.0 ± 3.3
"	M160	51.5 ± 3.6	4.1 ± 0.8	4.03 ± 0.42	4.42 ± 0.33	11.6 ± 1.9	0.685	37.6 ± 0.8
NGC4321	S250	$83. \pm 13.$	4.1 ± 1.7	2.08 ± 0.40	2.26 ± 0.50	10.4 ± 3.7	0.619	31.1 ± 1.7
"	M160	63.5 ± 3.4	3.7 ± 1.2	2.67 ± 0.20	2.92 ± 0.23	10.2 ± 1.7	0.681	30.6 ± 1.6
NGC4536	S250	$32. \pm 10.$	2.9 ± 1.2	3.6 ± 1.8	4.3 ± 1.5	$18. \pm 8.$	0.578	22.6 ± 3.1
"	M160	27.1 ± 4.4	3.4 ± 0.5	4.4 ± 1.3	4.7 ± 0.7	19.8 ± 3.2	0.591	20.8 ± 0.5
NGC4559	S250	7.71 ± 0.26	2.47 ± 0.42	2.1 ± 0.8	2.16 ± 0.22	9.5 ± 2.4	0.579	2.73 ± 0.15
"	M160	8.5 ± 1.2	2.7 ± 0.8	1.9 ± 0.9	1.89 ± 0.43	10.1 ± 2.1	0.541	2.65 ± 0.15
NGC4569	S250	12.9 ± 4.0	3.7 ± 0.6	1.9 ± 0.6	2.4 ± 0.7	14.2 ± 1.6	0.635	5.14 ± 0.25
"	M160	9.2 ± 0.8	3.4 ± 0.9	2.63 ± 0.36	3.12 ± 0.33	13.9 ± 1.6	0.694	4.71 ± 0.40
NGC4579	S250	$39. \pm 7.$	3.1 ± 0.9	1.55 ± 0.26	1.65 ± 0.28	7.9 ± 2.8	0.611	10.58 ± 0.32
"	M160	29.0 ± 1.0	2.9 ± 0.9	1.88 ± 0.07	2.066 ± 0.046	9.0 ± 1.6	0.675	9.83 ± 0.31
NGC4594	S250	16.4 ± 3.6	2.6 ± 1.4	1.06 ± 0.26	1.15 ± 0.24	6.2 ± 3.5	0.574	3.10 ± 0.16
"	M160	13.3 ± 1.0	2.6 ± 0.7	1.26 ± 0.11	1.34 ± 0.14	6.6 ± 0.9	0.619	2.94 ± 0.08
NGC4625	S250	1.47 ± 0.31	3.7 ± 0.9	2.1 ± 0.5	2.23 ± 0.49	9.2 ± 2.8	0.590	0.542 ± 0.025
"	M160	1.18 ± 0.21	4.2 ± 0.9	2.7 ± 0.8	2.6 ± 1.0	9.0 ± 3.7	0.625	0.512 ± 0.021
NGC4631	S250	28.4 ± 4.1	3.0 ± 0.5	4.4 ± 1.3	4.6 ± 1.4	10.9 ± 1.8	0.669	21.6 ± 1.4
"	M160	31.1 ± 2.9	2.90 ± 0.23	4.9 ± 0.6	4.3 ± 0.6	10.9 ± 1.0	0.631	22.0 ± 0.8
NGC4725	S250	$42. \pm 9.$	3.68 ± 0.49	0.90 ± 0.27	0.99 ± 0.23	5.7 ± 1.9	0.541	6.9 ± 0.7
"	M160	37.4 ± 3.7	3.6 ± 0.8	1.09 ± 0.16	1.09 ± 0.19	5.4 ± 2.6	0.566	6.72 ± 0.16
NGC4736	S250	8.5 ± 0.6	4.2 ± 0.6	4.0 ± 0.8	4.3 ± 0.6	7.0 ± 2.6	0.552	5.99 ± 0.34
"	M160	5.4 ± 0.5	3.70 ± 0.50	6.6 ± 1.7	6.5 ± 1.6	6.7 ± 1.8	0.642	5.8 ± 0.7
NGC4826	S250	4.0 ± 1.0	2.59 ± 0.39	5.5 ± 2.1	5.8 ± 1.3	6.5 ± 3.4	0.665	3.76 ± 0.16
"	M160	3.46 ± 0.30	2.57 ± 0.16	6.5 ± 1.3	6.5 ± 0.9	6.4 ± 3.6	0.673	3.67 ± 0.33
NGC5055	S250	$63. \pm 14.$	4.2 ± 0.8	1.70 ± 0.46	1.79 ± 0.40	7.8 ± 1.3	0.594	18.70 ± 0.44
"	M160	49.0 ± 3.0	3.89 ± 0.23	2.12 ± 0.17	2.28 ± 0.12	7.8 ± 3.8	0.659	18.4 ± 0.6
NGC5398	S250	0.69 ± 0.16	2.25 ± 0.37	1.4 ± 0.5	3.1 ± 0.8	28.0 ± 2.1	0.528	0.352 ± 0.013
"	M160	0.75 ± 0.22	1.8 ± 0.7	0.61 ± 1.42	2.4 ± 1.6	33.0 ± 4.8	0.488	0.297 ± 0.042
NGC5408	S250	0.049 ± 0.007	0.14 ± 0.28	8.5 ± 3.8	$21. \pm 6.$	$37. \pm 5.$	0.627	0.172 ± 0.016
"	M160	0.047 ± 0.017	0.14 ± 0.64	$10. \pm 6.$	$20. \pm 7.$	$39. \pm 5.$	0.661	0.154 ± 0.009
NGC5457	S250	$69. \pm 13.$	3.0 ± 0.6	1.58 ± 0.47	1.79 ± 0.42	12.4 ± 2.2	0.569	20.3 ± 1.2
"	M160	69.7 ± 2.0	3.0 ± 0.9	1.84 ± 0.35	1.77 ± 0.10	12.7 ± 1.8	0.550	20.3 ± 0.6
NGC5474	S250	1.5 ± 1.2	1.7 ± 0.8	1.5 ± 1.0	1.8 ± 0.9	6.9 ± 2.1	0.552	0.466 ± 0.043
"	M160	1.81 ± 0.29	2.10 ± 0.05	0.40 ± 0.10	1.49 ± 0.27	7.7 ± 1.2	0.489	0.442 ± 0.020
NGC5713	S250	$28. \pm 6.$	2.81 ± 0.41	6.8 ± 2.0	7.6 ± 2.1	17.5 ± 4.0	0.639	34.7 ± 3.8
"	M160	28.1 ± 2.4	2.74 ± 0.27	7.3 ± 1.9	7.2 ± 1.1	18.3 ± 3.3	0.610	33.3 ± 1.9
NGC5866	S250	9.4 ± 0.8	1.7 ± 0.9	3.36 ± 0.31	2.92 ± 0.33	1.3 ± 1.0	0.600	4.48 ± 0.21
"	M160	6.0 ± 0.5	1.6 ± 0.8	4.63 ± 0.41	4.54 ± 0.34	0.32 ± 0.61	0.692	4.46 ± 0.08
NGC6946	S250	$57. \pm 6.$	3.5 ± 0.8	3.4 ± 0.6	3.8 ± 0.6	13.5 ± 2.9	0.658	35.7 ± 3.2
"	M160	47.1 ± 4.1	3.5 ± 0.7	3.8 ± 0.6	4.4 ± 0.6	14.3 ± 2.9	0.688	34.1 ± 2.0
NGC7331	S250	$116. \pm 32.$	4.2 ± 0.9	2.3 ± 1.0	2.4 ± 1.0	7.6 ± 4.1	0.619	45.7 ± 4.0
"	M160	$97. \pm 9.$	3.95 ± 0.36	2.79 ± 0.44	2.73 ± 0.42	7.1 ± 1.8	0.641	43.7 ± 2.9
NGC7793	S250	5.5 ± 1.3	3.0 ± 0.9	1.9 ± 0.8	1.9 ± 0.7	8.1 ± 0.9	0.585	1.76 ± 0.13
"	M160	6.0 ± 0.8	3.2 ± 0.6	2.0 ± 0.9	1.8 ± 0.5	7.9 ± 2.5	0.545	1.78 ± 0.08
EIC3583	S250	1.75 ± 0.08	2.12 ± 0.13	1.53 ± 0.46	1.91 ± 0.32	8.3 ± 1.7	0.569	0.548 ± 0.041
"	M160	1.53 ± 0.23	2.3 ± 0.6	1.82 ± 0.42	2.05 ± 0.38	9.3 ± 0.9	0.523	0.514 ± 0.040
ENGC0586	S250	4.0 ± 1.0	3.873 ± 0.039	0.89 ± 0.62	1.0 ± 0.7	10.9 ± 2.2	0.549	0.67 ± 0.10
"	M160	2.31 ± 0.23	3.78 ± 0.12	1.50 ± 0.31	1.66 ± 0.18	8.6 ± 4.2	0.639	0.633 ± 0.022
ENGC1317	S250	11.3 ± 1.5	3.0 ± 0.7	4.1 ± 1.5	3.7 ± 0.9	4.2 ± 0.8	0.596	6.9 ± 0.6
"	M160	7.6 ± 0.7	3.13 ± 0.28	5.0 ± 1.0	5.1 ± 0.9	3.9 ± 2.2	0.687	6.34 ± 0.38
ENGC1481	S250	0.94 ± 0.15	1.5 ± 1.4	5.9 ± 3.7	6.0 ± 2.1	16.1 ± 2.8	0.567	0.93 ± 0.11
"	M160	0.95 ± 0.24	2.3 ± 1.7	3.6 ± 3.2	5.9 ± 2.4	18.6 ± 4.0	0.578	0.93 ± 0.10
ENGC1510	S250	0.244 ± 0.048	0.60 ± 0.35	4.0 ± 2.9	8.5 ± 3.4	35.1 ± 3.8	0.569	0.339 ± 0.011
"	M160	1.16 ± 0.20	0.70 ± 0.26	0.47 ± 0.12	1.94 ± 0.37	34.9 ± 1.6	0.465	0.367 ± 0.014
ENGC3187	S250	7.5 ± 1.8	1.80 ± 0.48	1.2 ± 1.0	1.4 ± 1.0	11.6 ± 1.8	0.541	1.75 ± 0.21
"	M160	9.1 ± 0.9	2.92 ± 0.30	0.56 ± 0.55	1.12 ± 0.26	11.4 ± 3.5	0.476	1.67 ± 0.13
ENGC4533	S250	1.49 ± 0.27	2.4 ± 0.5	1.5 ± 0.8	1.6 ± 0.7	6.4 ± 2.5	0.538	0.393 ± 0.048
"	M160	1.183 ± 0.043	2.3 ± 0.5	1.5 ± 0.5	1.83 ± 0.16	8.2 ± 1.5	0.534	0.355 ± 0.021
ENGC7335	S250	$54. \pm 7.$	1.6 ± 0.5	1.35 ± 0.42	1.49 ± 0.36	5.6 ± 2.1	0.573	13.1 ± 1.6
"	M160	38.2 ± 2.9	2.1 ± 0.5	1.9 ± 0.5	2.0 ± 0.5	6.7 ± 3.6	0.608	12.3 ± 1.3
ENGC7337	S250	$66. \pm 30.$	3.51 ± 0.13	0.59 ± 0.27	0.68 ± 0.23	8.6 ± 1.5	0.490	7.4 ± 0.7
"	M160	$30. \pm 6.$	3.1 ± 1.2	1.25 ± 0.31	1.45 ± 0.40	7.3 ± 5.4	0.589	7.0 ± 0.9

a Renormalized as described in §5.2.

Table 10. Gas Masses for M160 Resolution Galaxy Mask and Dust/Gas Ratio

Galaxy	$M(\text{H I})^a$ ($10^9 M_\odot$)	$M(\text{H}_2)^a$ ($10^9 M_\odot$)	$M_{\text{dust}}{}^b$ ($10^6 M_\odot$)	$M_{\text{dust}}/M_{\text{H}}{}^a$
DDO053	0.0382 ± 0.0038	···	< 0.21	< 0.0060
DDO154	0.128 ± 0.013	< 0.0010	< 0.61	< 0.0053
DDO165	0.069 ± 0.007	···	< 0.52	< 0.0085
Hol1	0.0366 ± 0.0037	< 0.00077	< 0.67	< 0.020
Hol2	0.232 ± 0.023	< 0.0016	0.112 ± 0.006	< 0.00057
IC342	14.3 ± 4.3	···	41.28 ± 0.21	< 0.0041
IC2574	0.87 ± 0.09	0.0084 ± 0.0014	0.782 ± 0.019	0.00089 ± 0.00012
M81dwB	0.0079 ± 0.0008	< 0.00057	< 0.081	< 0.012
NGC0337	4.13 ± 0.41	0.389 ± 0.042	15.67 ± 0.32	0.0035 ± 0.0005
NGC0584	0.157 ± 0.047	···	< 1.59	< 0.014
NGC0628	2.30 ± 0.23	1.38 ± 0.14	21.44 ± 0.08	0.0058 ± 0.0012
NGC0855	0.115 ± 0.034	···	< 1.02	< 0.013
NGC0925	4.45 ± 0.45	0.256 ± 0.027	13.19 ± 0.17	0.0028 ± 0.0004
NGC1097	4.4 ± 1.3	···	73.3 ± 0.7	< 0.024
NGC1266	> 0.0095	···	12.14 ± 0.29	< 1.31
NGC1291	1.32 ± 0.39	···	13.63 ± 0.23	< 0.015
NGC1482	0.67 ± 0.20	···	22.5 ± 0.6	< 0.050
NGC1512	2.9 ± 0.9	···	12.10 ± 0.13	< 0.0060
NGC2146	3.3 ± 1.0	8.5 ± 0.9	55.9 ± 0.6	0.0047 ± 0.0014
NGC2798	0.96 ± 0.10	2.52 ± 0.25	15.95 ± 0.44	0.0046 ± 0.0014
NGC2841	6.6 ± 0.7	0.89 ± 0.09	48.42 ± 0.30	0.0064 ± 0.0009
NGC2915	0.35 ± 0.11	···	0.039 ± 0.006	< 0.00018
NGC2976	0.142 ± 0.014	0.073 ± 0.007	1.948 ± 0.031	0.0090 ± 0.0019
NGC3049	1.01 ± 0.10	0.144 ± 0.018	6.84 ± 0.21	0.0059 ± 0.0010
NGC3077	0.429 ± 0.043	0.0161 ± 0.0017	1.425 ± 0.018	0.0032 ± 0.0004
NGC3184	3.68 ± 0.37	1.98 ± 0.20	31.91 ± 0.27	0.0056 ± 0.0011
NGC3190	0.46 ± 0.14	0.058 ± 0.013	18.2 ± 0.5	0.035 ± 0.012
NGC3198	8.1 ± 0.8	0.62 ± 0.06	26.71 ± 0.30	0.0031 ± 0.0004
NGC3265	0.17 ± 0.05	···	2.00 ± 0.24	< 0.018
NGC3351	1.08 ± 0.11	1.02 ± 0.10	16.34 ± 0.15	0.0078 ± 0.0018
NGC3521	10.4 ± 1.0	4.18 ± 0.42	82.6 ± 0.9	0.0057 ± 0.0011
NGC3621	5.2 ± 0.5	···	20.75 ± 0.27	< 0.0045
NGC3627	1.12 ± 0.11	3.02 ± 0.30	42.22 ± 0.20	0.0102 ± 0.0029
NGC3773	0.109 ± 0.033	···	0.689 ± 0.024	< 0.0093
NGC3938	5.1 ± 0.5	2.51 ± 0.25	48.42 ± 0.32	0.0063 ± 0.0012
NGC4236	1.91 ± 0.19	0.0028 ± 0.0010	1.77 ± 0.06	0.00092 ± 0.00012
NGC4254	4.93 ± 0.49	7.2 ± 0.7	69.99 ± 0.42	0.0058 ± 0.0015
NGC4321	3.38 ± 0.34	6.9 ± 0.7	81.16 ± 0.39	0.0079 ± 0.0021
NGC4536	4.62 ± 0.46	1.86 ± 0.19	29.5 ± 0.6	0.0045 ± 0.0009
NGC4559	3.16 ± 0.32	0.051 ± 0.006	7.90 ± 0.14	0.0025 ± 0.0003
NGC4569	0.248 ± 0.025	1.30 ± 0.13	11.88 ± 0.16	0.0077 ± 0.0024
NGC4579	0.73 ± 0.07	2.42 ± 0.24	32.95 ± 0.11	0.0105 ± 0.0030
NGC4594	0.20 ± 0.06	0.043 ± 0.007	12.57 ± 0.11	0.023 ± 0.008 [c]
NGC4625	0.241 ± 0.024	0.0285 ± 0.0039	1.365 ± 0.046	0.0051 ± 0.0008
NGC4631	7.7 ± 0.8	1.62 ± 0.16	36.84 ± 0.30	0.0040 ± 0.0006
NGC4725	3.51 ± 0.35	0.67 ± 0.07	34.40 ± 0.20	0.0082 ± 0.0013
NGC4736	0.50 ± 0.05	0.59 ± 0.06	6.676 ± 0.034	0.0061 ± 0.0015
NGC4826	0.112 ± 0.011	0.66 ± 0.07	4.66 ± 0.06	0.0060 ± 0.0019
NGC5055	3.70 ± 0.37	3.35 ± 0.33	57.54 ± 0.27	0.0082 ± 0.0018
NGC5398	0.26 ± 0.08	···	0.593 ± 0.038	< 0.0035
NGC5408	0.24 ± 0.07	···	0.0603 ± 0.0049	< 0.00039
NGC5457	11.5 ± 1.1	2.58 ± 0.26	69.15 ± 0.17	0.0049 ± 0.0008
NGC5474	0.62 ± 0.06	< 0.0049	1.429 ± 0.035	< 0.0026
NGC5713	3.24 ± 0.32	4.00 ± 0.40	34.1 ± 0.6	0.0047 ± 0.0012
NGC6946	3.52 ± 0.35	6.6 ± 0.7	63.46 ± 0.30	0.0063 ± 0.0017
NGC7331	10.7 ± 1.1	5.2 ± 0.5	$116. \pm 1.$	0.0073 ± 0.0014
NGC7793	0.99 ± 0.10	···	5.75 ± 0.05	< 0.0065

[a] He is not included.

[b] Renormalized as described in §5.2.

[c] M_{H} includes $M = 2.9 \times 10^8 M_\odot$ of hot gas (Li et al. 2011)

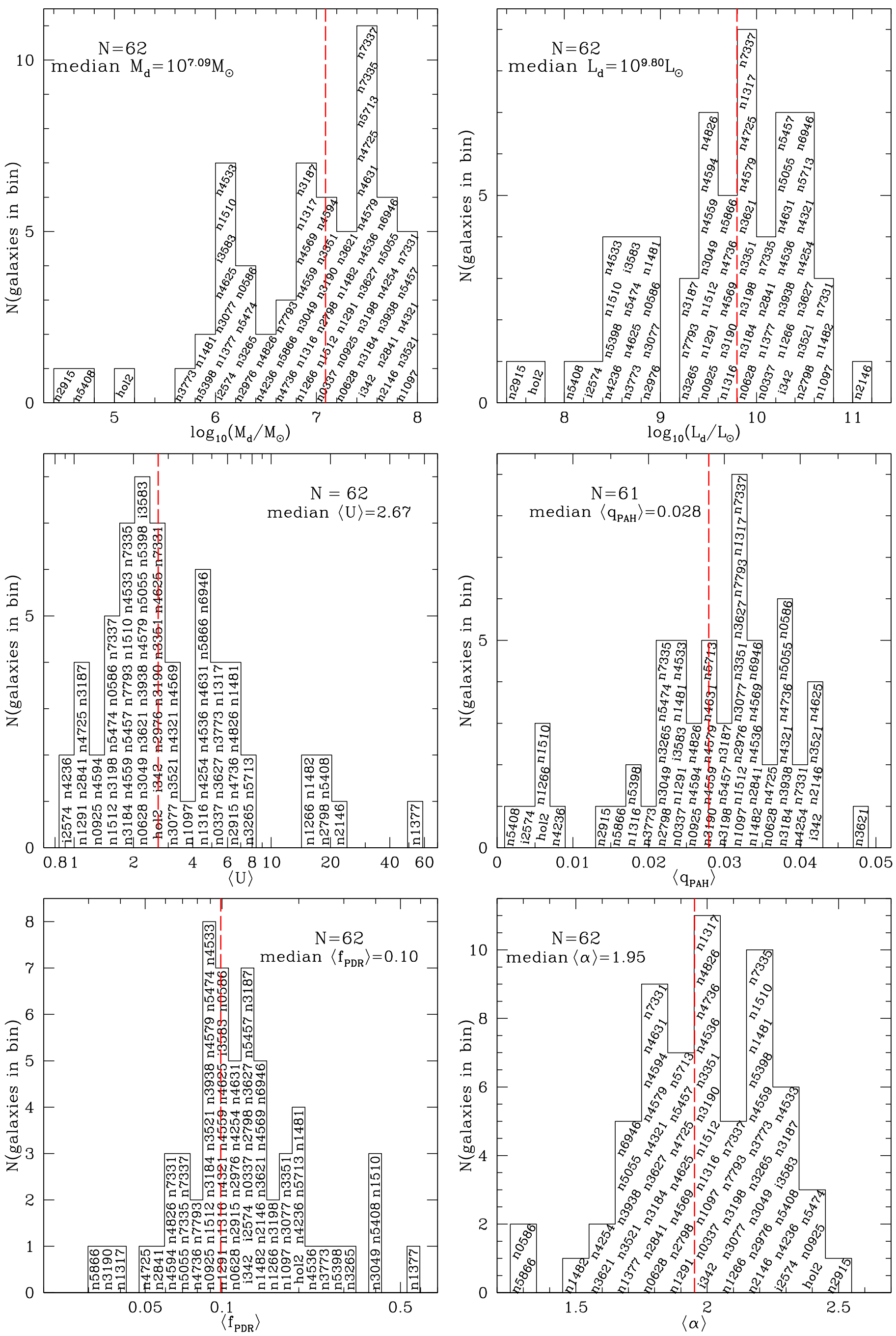

Figure 6. Distributions of dust and starlight parameters for the KF62 sample. NGC 1377 is omitted from the $q_{\rm PAH}$ histogram (see text). $M_{\rm d}$ and $\langle U\rangle$ are renormalized values.

of the fit to the observed SED, but in most cases the fit quality does not suffer greatly if α is held fixed at $\alpha = 2$, reducing the number of free parameters. Recall that $\alpha = 2$ corresponds to equal amounts of dust power per logarithmic interval in starlight intensity U.

Compared with the "gold standard", modeling using PSFs smaller than M160, and hence having fewer cameras available, can affect the derived dust and starlight parameters. As the PSF shrinks, data are provided by fewer cameras, the wavelength coverage shrinks as the PSF is reduced below S500, and the photometry becomes noisier because it is being smoothed over smaller PSFs. Above we have compared two cases: modeling with the M160 PSF, versus modeling with the S250 PSF, but additional comparisons are made in Appendix D. Here we simply note some trends. In general $M_{\rm d}$ is fairly robust: the S250 modeling typically overestimates $M_{\rm d}$ by $\sim$25%, but agrees with the "gold standard" to within a factor 1.5 for over 75% of the galaxies (see Fig. 19). $q_{\rm PAH}$ estimates are also robust, with typical changes of less than 15%. Longer wavelength coverage (SPIRE350 and SPIRE500) gives more reliable dust estimates. Even comparing resolved and global modeling of dust properties can give different results; although most parameters are consistent to within a few percent, global modeling can underestimate $M_{\rm d}$ by as much as 35%, as for NGC 1481 and NGC 3077 (see Figure 21). This is because the resolved models can have "cold" regions with low $U_{\rm min}$ values that contribute to dust mass estimates but do not emerge in the global results (e.g. Galliano et al. 2011; Galametz et al. 2012).

6.5. *Dependence of global PAH fraction on metallicity*

Figure 7a shows $q_{\rm PAH}$ vs. log(O/H) for 51 galaxies using direct determinations of (O/H) where available (5 galaxies), and PT estimates otherwise. 19 galaxies have been omitted: 8 dust nondetections have been excluded, NGC1377 (a dense starburst with a core that is optically thick at 8μm – see Section 6.3.2), plus 10 galaxies for which we have no PT estimate for O/H. The oxygen abundance in these galaxies ranges over more than a factor of 10, and $q_{\rm PAH}$ shows a clear tendency to increase with increasing O/H, although there is considerable scatter. The observed behavior can be approximated by a step function, with an abrupt increase in $q_{\rm PAH}$ when $12+\log_{10}({\rm O/H})_{\rm PT}$ rises above $\sim$8.0 Alternatively, $q_{\rm PAH}$ can be approximated by a linear dependence on log(O/H). Best-fit step function and linear function are shown in Fig. 7a, with χ^2 per degree of freedom of 8.0 and 6.6, respectively.

Figure 7b shows $q_{\rm PAH}$ vs. the PP04N2 estimate for metallicity. Again, we show both step functions and a linear dependence on $\log_{10}$(O/H). In this case, the function linear in $\log({\rm O/H})_{\rm PP04N2}$ gives a much better fit to the data:

$$q_{\rm PAH} \approx 0.0396\,[(12+\log_{10}({\rm O/H})_{\rm PP04N2}) - 7.94] \quad (18)$$

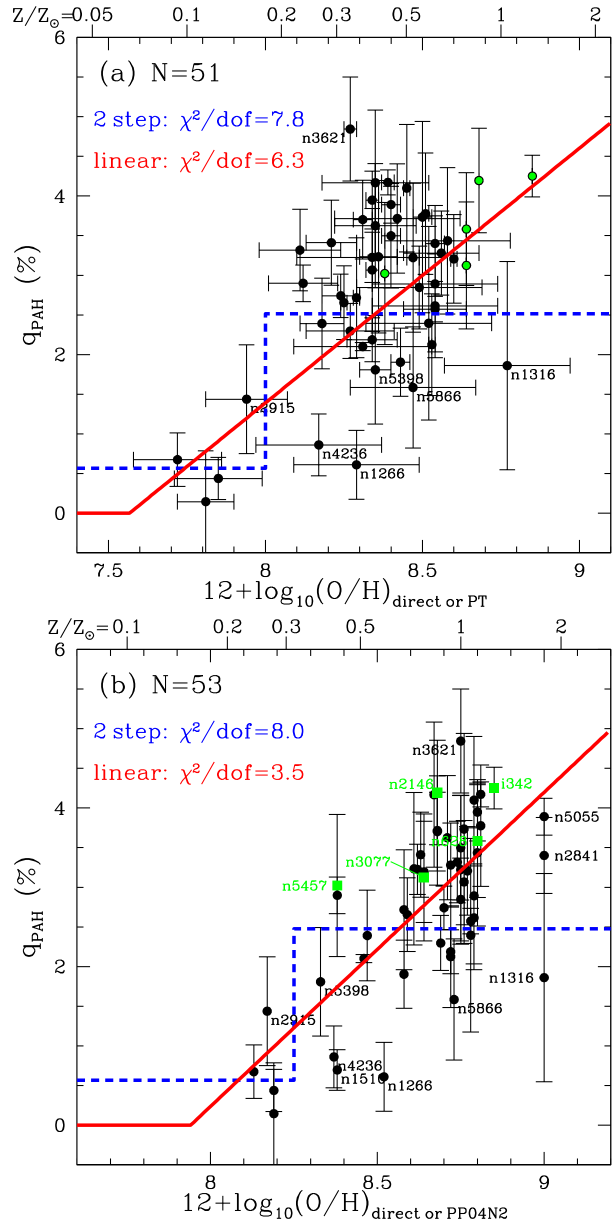

Figure 7. (a) PAH abundance parameter $q_{\rm PAH}$ versus oxygen abundance (direct or PT) for 51 galaxies (see text). Two $q_{\rm PAH}$ estimators are shown: one is a step function, and the other is linear above a threshold value. Selected galaxies have been labeled. The step function and linear estimators have similar χ^2/dof =7.8 and 6.3. (b) Same but for PP04N2 oxygen abundance, now for 52 galaxies (a PP04N2 oxygen abundance is available for NGC 1512). The 5 galaxies where O/H has been determined by "direct" methods are shown in green. The linear fit of $q_{\rm PAH}$ vs. $12+\log_{10}({\rm O/H})$ (Eq. 18) gives an improved fit, with $\chi^2/{\rm dof} = 3.5$, and a threshold $({\rm O/H}) \approx 0.15({\rm O/H})_\odot$.

(for $12 + \log_{10}(\mathrm{O/H})_{\mathrm{PP04N2}}$>7.94). This fit, with 53-2=51 degrees of freedom (dof), has χ^2/dof= 3.5: the PP04N2 metallicity is evidently a *much* better predictor of q_{PAH} than is the PT metallicity.[9] This strongly suggests that the PP04N2 metallicities are more tightly related to the properties of the ISM – including metallicity – that regulate the balance between PAH formation and destruction.

The observed tendency for q_{PAH} to increase with increasing metallicity is consistent with many previous studies. The connection between PAH abundance and metallicity was first noted in ground-based spectroscopy by Roche et al. (1991), and further investigated using ISO data (Boselli et al. 1998; Sturm et al. 2000; Madden 2000). Hunt et al. (2005, 2010) found PAH emission to be weak in low-metallicity blue compact dwarf galaxies. Engelbracht et al. (2005) used IRAC and MIPS24 photometry to show that there was an abrupt drop in the 8μm/24μm flux ratio when the metallicity dropped below 8.2, interpreting this as due to a sharp drop in the abundance of PAHs that normally dominate the emission at 8μm. Draine et al. (2007) estimated q_{PAH} for 61 SINGS galaxies, using the DL07 model with IRAC and MIPS photometry, and found a similar result: a sharp increase in q_{PAH} when $12 + \log_{10}(\mathrm{O/H})_{\mathrm{PT}}$ rises above $\sim$8.2.

Nevertheless, there are outliers in Fig. 7b. The SB0 galaxy NGC 1266 has $q_{\mathrm{PAH}} = 0.70\%$, unusually low for a galaxy with $12 + \log_{10}(\mathrm{O/H})_{\mathrm{PP04N2}}$=8.51. The *Spitzer* and *Herschel* photometry of NGC 1266 (see Fig. 17.8) appears to be reliable. Because the optical spectrum of NGC 1266 is AGN-dominated, the metallicity is not based on emission lines, and is therefore highly uncertain. Moustakas et al. (2010) estimated the metallicity from an assumed luminosity-metallicity relation. The resulting $12+\log_{10}(\mathrm{O/H})_{\mathrm{PP04N2}}$=8.51 is consistent with the stellar mass-metallicity relation (Andrews & Martini 2013). Perhaps the PAH abundance in this galaxy has been suppressed by phenomena associated with the active galactic nucleus (AGN) that is driving a molecular outflow characterized by shocked gas (Alatalo et al. 2011; Pellegrini et al. 2013; Alatalo et al. 2015).

The SAB0 galaxy NGC 1316 = Fornax A is another outlier. The dust emission is weak relative to the starlight, making the q_{PAH} estimate uncertain. In addition, the starlight heating the dust is likely from an old population, similar to the bulge of M31, and our estimate of q_{PAH} (based on single-photon heating by starlight assumed to have the solar neighborhood spectrum) would then be biased low. The estimate for q_{PAH} in the center of M31 increases by almost a factor of two when calculated using the correct starlight spectrum (Draine et al. 2014), and a similar correction might bring q_{PAH} for NGC 1316 closer to the general trend in Figure 7b. In addition, the high metallicity estimated for NGC 1316 may be influenced by the AGN contribution to the emission line spectrum.

[9] For some galaxies we use "direct" metallicities rather than the PT or PP04N2 weak-line estimates, but χ^2 is dominated by the 51 galaxies where we use PP04N2 instead of the PT metallicity estimate.

In Figure 7 it is striking that the bulk of the galaxies with $12+\log_{10}(\mathrm{O/H})_{\mathrm{PP04N2}}> 8.3$ have q_{PAH} in the 1.5–5% range. Evidently the physical processes responsible for formation and destruction of PAHs in normal star-forming galaxies tend to maintain PAH abundances near 3% provided that the metallicity $Z/Z_\odot \gtrsim 0.3$. From Eq. (18) it appears that there is a threshold metallicity for PAH formation: $q_{\mathrm{PAH}} \approx 0$ for $12+\log_{10}(\mathrm{O/H})_{\mathrm{PP04N2}} \lesssim 7.94$, or $Z/Z_\odot \lesssim 0.15$.

6.6. *Dependence of global dust-to-gas ratio on metallicity*

6.6.1. *Theoretical Expectations*

The abundance of dust in the ISM is the result of competition between processes that form dust (dust formation in stellar outflows, and dust growth in the ISM) and processes that return material to the gas phase (e.g., sputtering in hot gas, and vaporization in high-speed grain-grain collisions). In the Milky Way and other star-forming galaxies with near-solar metallicity, accretion of atoms onto grains is rapid in the cool, dense phases of the ISM, and the balance between grain growth and grain destruction maintains a large fraction of the refractory elements in grains. Most of the dust in the Milky Way must have been grown in the ISM – there is simply no other way to understand the observed extreme depletions of elements like Si, Al, Ca, Ti, and Fe in the diffuse ISM (see, e.g., Draine 1990; Weingartner & Draine 1999; Draine 2009).

The black dashed line in Fig. 8a shows the expected dependence of $M_{\mathrm{d}}/M_{\mathrm{H}}$ on O/H if all galaxies had heavy element abundances proportional to solar abundances, and the same depletion pattern as measured in the well-studied cloud toward the nearby star ζOph; in this cloud the refractory elements (e.g., Mg, Si, Fe...) are almost completely incorporated into grains, and we infer a dust/H mass ratio 0.0099 (see Table 23.1 of Draine 2011). For this scenario, we then expect

$$\left(\frac{M_{\mathrm{d}}}{M_{\mathrm{H}}}\right) = 0.0099 \left(\frac{Z}{Z_\odot}\right) \quad , \qquad (19)$$

where we take $Z/Z_\odot = 1$ for $12+\log_{10}(\mathrm{O/H})$=8.72 (Asplund et al. 2009, corrected for diffusion). However, in the overall ISM, $M_{\mathrm{d}}/M_{\mathrm{H}}$ will fall below this limiting value, because of dust destruction processes.

A simple toy model can illustrate the competition between formation and destruction processes. (Similar models have been discussed by, e.g., Edmunds 2001; Mattsson et al. 2012; Asano et al. 2013).

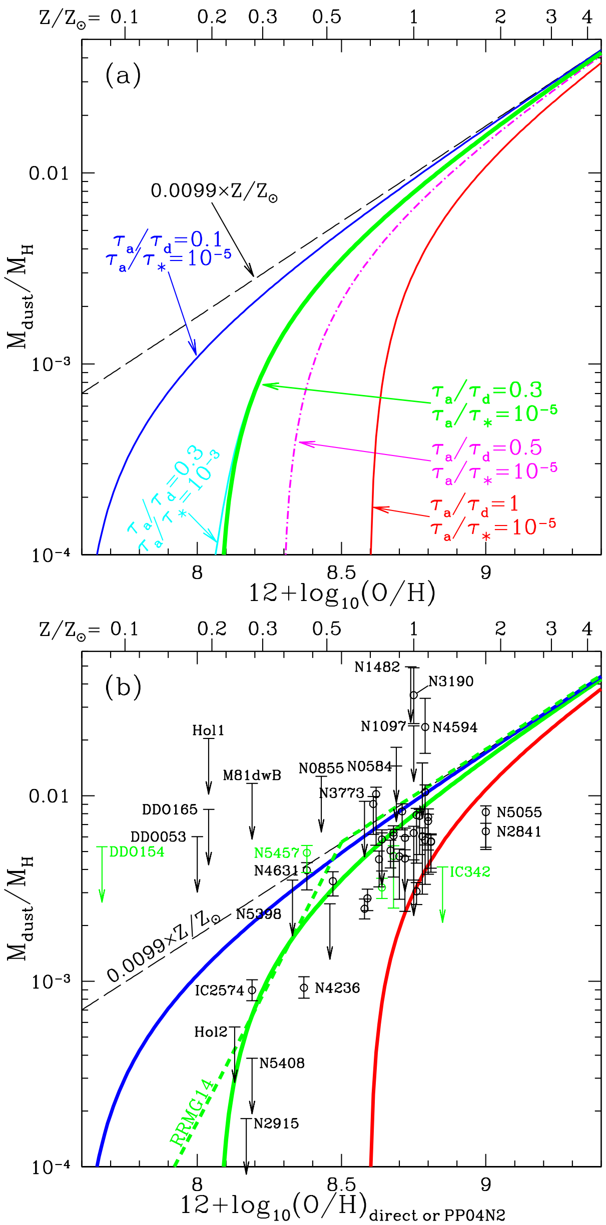

Figure 8. (a) Dust/H mass ratio vs. metallicity for the toy model (Eq. 21) for selected values of τ_a/τ_d and $\tau_a/\tau_\star$ (see text). (b) Measured $M_{\rm d}/M_{\rm H}$ (for the M160 resolution galaxy mask), versus $12+\log_{10}({\rm O/H})$ (see text) for 57 KINGFISH galaxies. Selected galaxies have been labeled. Arrows indicate upper limits for the 16 galaxies lacking CO data. The green curve is Eq. (21) for $\tau_a/\tau_d = 0.3$ and $\tau_a/\tau_\star \lesssim 10^{-3}$; the blue and red curves are for $\tau_a/\tau_d = 0.1$ and 1. The green dashed line is the broken power-law fit from Rémy-Ruyer et al. (2014).

Let Z_m be the fraction of the ISM mass in "refractory" elements ($Z_m \approx 0.007 \times (Z/Z_\odot) = 0.007 \times 10^{(12+\log_{10}({\rm O/H})-8.75)}$), and Z_d be the fraction of the ISM mass in dust grains made of these refractory elements ($M_{\rm d}/M_{\rm H} = 1.4Z_d$). Clearly $Z_d < Z_m$, since some of the refractory elements are in the gas phase.

Destruction and grain growth in the ISM both contribute to the rate of change of Z_d. We also include a term representing injection of solid grains into the ISM from stellar sources (AGB stars, supernovae, etc.). The rate of change of Z_d is given by

$$\dot{Z}_d = -\frac{Z_d}{\tau_d} + \frac{(Z_d/0.007)}{\tau_a}\left(Z_m - Z_d\right) + \frac{Z_m}{\tau_\star} \quad . \tag{20}$$

The first term $-Z_d/\tau_d$ is the rate of dust destruction: τ_d is the lifetime of solid material in the ISM against destructive processes that return material to the gas phase. The destruction rate τ_d^{-1} is a mass-weighted average over the dust in the multiphase ISM. Studies of the effects of supernova blastwaves in the local ISM suggest timescales $\tau_d \approx 4 \times 10^8\,{\rm yr}$ (see discussion in, e.g., Draine 2009). Realistic estimation of τ_d requires a detailed dynamic multiphase model of the ISM (e.g., Zhukovska et al. 2016). The appropriate value of τ_d will obviously vary with galactocentric radius within a galaxy, and from galaxy to galaxy.

The term in Eq. (20) representing grain growth is proportional to $Z_d(Z_m - Z_d)$ because it depends on grain surface area ($\propto Z_d$, for a fixed distribution of grain sizes) and on the gas-phase abundance of condensible elements ($\propto (Z_m - Z_d)$). $(Z_d/0.007)\tau_a^{-1}$ is the probability per unit time that a refractory atom in the gas phase will collide with and stick to a grain.

The last term, $Z_m/\tau_\star$, represents injection of dust into the ISM from stellar sources, such as cool AGB stars, planetary nebulae, and core-collapse supernovae. This term will obviously depend on the stellar populations. Here, for illustration, we take the injection rate to be proportional to the metallicity Z_m. For galaxies of interest here, this injection term is small compared to the other terms in Eq. (20), and the precise form adopted in Eq. (20) is not critical.

If the shortest of the time scales $\{\tau_a, \tau_d\}$ is short compared to the $\sim\!10^9\,{\rm yr}$ timescale for galactic chemical evolution, and $\tau_\star \gg \{\tau_a, \tau_d\}$, we can neglect time-dependence of the metallicity Z_m. The toy model will approach a quasi steady-state solution with $\dot{Z}_d \approx 0$:

$$Z_d = \frac{1}{2}\left(Z_m - \frac{0.007}{\tau_d/\tau_a}\right) + \frac{1}{2}\left[\left(Z_m - \frac{0.007}{\tau_d/\tau_a}\right)^2 + \frac{0.028}{\tau_\star/\tau_a} Z_m\right]^{1/2} \quad . \tag{21}$$

This solution for Z_d depends only on Z_m and on ratios of time scales, τ_a/τ_d and $\tau_\star/\tau_d$. Eq. (21) for Z_d is plotted in Fig. 8a for several choices of the ratios τ_a/τ_d and $\tau_a/\tau_\star$. Note that for all of our examples we take $\tau_\star^{-1} \ll \tau_a^{-1}$: dust formation in stellar outflows is secondary to dust growth in the ISM (i.e., only a small fraction of interstellar dust is "stardust"). For large values of Z_m, all models approach the upper limit $Z_d/Z_m = 1$ (long-dashed line in Fig. 8b).

Models of interest have $\tau_a < \tau_d$, so that for near-solar abundances, accretion is faster than destruction, and a solar-metallicity ISM can maintain a large fraction of the refractory elements in dust (i.e., $Z_d/Z_m \gtrsim 0.5$). However, for sufficiently low O/H, accretion rates become slow, resulting in low values of Z_d/Z_m.

6.6.2. *Observations*

Using dust mass estimates based on modeling the infrared emission, radial variations in dust-to-gas ratios (DGRs) were found for galaxies in the SINGS sample (Muñoz-Mateos et al. 2009) and for M101 (Vílchez et al. 2019). The dust-to-metals ratio was approximately constant for KK04 metallicities $12 + \log_{10}(\mathrm{O/H})_{\mathrm{KK}} \geq 9.0$, but for $12+\log_{10}(\mathrm{O/H})_{\mathrm{KK}} \leq 8.8$ the dust-to-metals ratio appeared to decline with decreasing metallicity. Chiang et al. (2018) found variations in the dust-to-metals ratio in M101, which they related to both variations in metallicity and H_2 fraction. De Cia et al. (2016) found similar behavior in a sample that included 55 damped Lyman alpha systems (DLAs), where dust abundances were inferred from depletions of Si, and metallicities from [Zn/Fe]. It appears that as metallicity decreases below a certain threshold (e.g., $12 + \log_{10}(\mathrm{O/H})_{\mathrm{KK}} < 8.8$), an increasing fraction of refractory elements (Mg, Si, Fe, ...) remains in the gas phase.

Dust-to-gas ratios (DGRs) for the KF57 sample (see Table 1) are plotted against O/H in Fig. 8b, with dust masses estimated from our model, gas masses taken from Table 10, and the PP04N2 estimate for O/H. 14 galaxies have detections of both dust and H I, but were either not observed or not detected in CO, resulting in DGR upper limits. An additional 7 galaxies were detected in H I but not in dust, resulting in DGR upper limits.

Figure 8b shows a clear dependence of dust/gas ratio on metallicity. With some exceptions, the observed dust/H mass ratios for the KF57 sample are in broad agreement with the toy model (Eq. 19) for $0.1 \lesssim \tau_a/\tau_d \lesssim 1$, with $\tau_a/\tau_d = 0.3$ (green curve in Fig. 8b) providing a reasonable fit to the main trend in $M_{\mathrm{d}}/M_{\mathrm{H}}$ vs O/H.

We do not expect all galaxies to be characterized by a single value of τ_a/τ_d. Allowing for reasonable variation of τ_a/τ_d from galaxy to galaxy (ranging from $\tau_a/\tau_d = 1$ for the red curve to $\tau_a/\tau_d = 0.1$ for the blue curve) can accommodate almost all of the measured values. However, there are some notable exceptions:

- NGC 1482 (type SA0), This galaxy with near-solar O/H has a measured dust/H mass ratio several times larger than the "upper limit" $0.0099(Z/Z_\odot)$ (although NGC 1482 is missing CO measurements). It is notable that the ISM appears to have been subject to unusual activity. NGC 1482 shows evidence of a galactic-scale "superwind": the X-ray morphology shows a striking "hourglass" shape emerging from the plane of the disk (Strickland et al. 2004; Vagshette et al. 2012). Interestingly, this galaxy is completely missing H I in its central region, with atomic gas only found in two blobs ~2 kpc distant from its center, roughly at the confines of the X-ray emission (Hota & Saikia 2005). CO observations of NGC 1482 are needed. If NGC 1482 were found to have $M(\mathrm{H}_2) + M(\mathrm{H\,II}) \approx 1.3 \times 10^9 M_\odot$, the $M_{\mathrm{d}}/M_{\mathrm{H}}$ ratio would be normal for its metallicity.
- NGC 4594 (M104 "Sombrero", type SAb) also has near-solar O/H, but a dust/H mass ratio several times larger than the expected upper limit $0.0099(Z/Z_\odot)$. NGC 4594 has diffuse X-ray emission, suggesting the presence of a galactic-scale outflow (Li et al. 2011). Li et al. (2011) estimate the hot gas to have a temperature $T \approx 6 \times 10^6$ K and total mass $M_{\mathrm{hot}} \approx 2.9 \times 10^8 M_\odot$. Adding this to the Bajaja et al. (1984) value for H I, and the H_2 mass estimated with a standard X_{CO} factor, we find $M_{\mathrm{H}} = 6.0 \times 10^8 M_\odot$, and $M_{\mathrm{d}}/M_{\mathrm{H}} = 0.023$, about a factor of 2.5 above the ratio expected for metallicity $Z/Z_\odot \approx 1$. The gas in the hot phase, with a density $n_{\mathrm{H}} \approx 0.1\,\mathrm{cm}^{-3}$, has a cooling time $\tau \approx 5 \times 10^7$ yr (Li et al. 2011). Some of the hot gas may have cooled down to $\sim 10^4$ K, perhaps making an additional contribution to the total gas mass present in NGC 4594. We suggest that NGC 4594 may contain a substantial mass of diffuse H II at $\sim 10^4$ K that has not yet been detected.

Gravity, radiation pressure, and inertia can all lead to velocity differences between gas and dust, allowing the two to separate. However, because dust is generally well-coupled to the gas by both gas drag and the Lorentz force on charged grains, gas-grain "slip" velocities are generally small (e.g., Weingartner & Draine 2001b), and scenarios where gas is removed but dust is left behind are not viable unless the gas flows are slow enough that the small gas-grain "slip" velocities suffice to prevent the dust grains from leaving the galaxy. Even if gas is stripped or lost in an outflow, we expect the metallicity in the remaining gas [and therefore the upper bound Eq. (19) on the dust/mass ratio] to be unaffected. If NGC 1482 and NGC 4594 truly have high dust/gas ratios, then this would appear to require a mechanism for concentrating the dust in part of the gas, and removing the dust-poor gas via an outflow or stripping. Alternatively, perhaps the dust/gas ratio is actually normal, but the dust mass has been overestimated because the dust material for some reason has a far-infrared/submm opacity that is significantly larger than found in normal star-forming galaxies. The

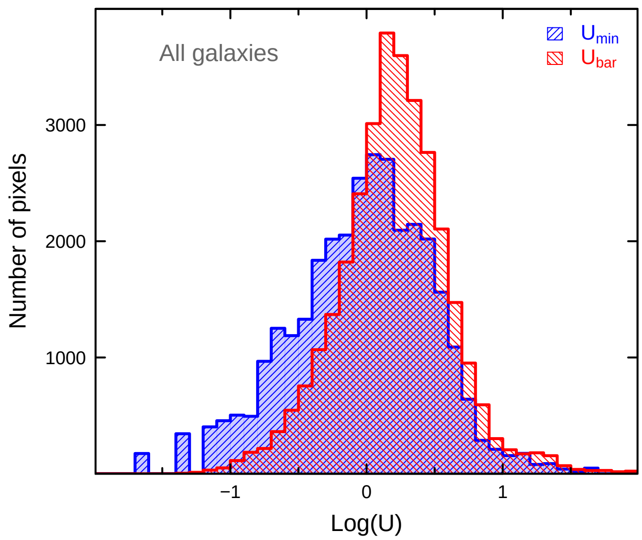

Figure 9. Distributions of $U_{\rm min}$ and $\overline{U}$ ($U_{\rm bar}$) for all galaxies. $U_{\rm min}$ and $\overline{U}$ are the renormalized values (see Eq. 13-16). Both distributions are fairly broad; for a given pixel, $\overline{U}-U_{\rm min}$ may be smaller than or comparable to $U_{\rm min}$ given that $f_{\rm PDR}$ is usually modest. Thus, it is not surprising that the two peaks are similar.

elevated dust/gas mass ratios in NGC 1482 and NGC 4594 require further study.

- NGC 2841 (Type SAb) and NGC 5055 (M63, Type SAbc): These two galaxies have much *lower* dust/gas ratios than would be expected given their high estimated metallicities ($12+\log_{10}({\rm O/H})_{\rm PP04N2}=9.31$: $Z/Z_\odot=3.6$). The photometry for these galaxies is reliable, and the models reproduce the SED out to 500μm. However, it seems likely that the metallicities given in Table 2 are overestimated. Moustakas et al. (2010) with KK04 found that NGC 2841 and NGC 5055 have $12+\log_{10}({\rm O/H})$ significantly greater than 9, $\sim$0.2 dex higher than the values found for the central regions in the same galaxies by Pilyugin et al. (2014). Pilyugin et al. (2014) also deduce strong metallicity gradients in these two galaxies implying that at $0.5\,R_{25}$, the characteristic $12+\log_{10}({\rm O/H})\sim8.6$. Such metallicities, better representing the average over the galactic disk, would be consistent with the observed dust/gas ratios for these two galaxies.

In Fig. 8b we also show the broken power-law empirical trend found by Rémy-Ruyer et al. (2014), with $M_{\rm d}/M_{\rm H}\propto({\rm O/H})$ for O/H above a critical value,[10] but with $M_{\rm d}/M_{\rm H}\propto({\rm O/H})^{3.02}$ for lower values of (O/H). This empirical result is seen to fall close to our toy model with $\tau_a/\tau_d=0.3$.

6.7. *Resolved trends of DL07 parameters*

Using data at M160 resolution, the synergy of *Herschel* and *Spitzer* for the KINGFISH sample enables an assessment of dust properties on kpc scales in nearby galaxies (the FWHM of the M160 PSF, 38.″8, corresponds to 1.86 kpc at the median KINGFISH sample distance of 9.9 Mpc). The number of M160 18″×18″ pixels in each galaxy ranges from 20 for the smallest galaxies (M81 dwB, NGC 584) to >4000 pixels for the largest ones (NGC 5457 = M 101 and IC 342); the resolved sample as a whole, including the nine "extra" galaxies, comprises >32 000 pixels with well-defined dust parameters and photometry.

Figure 9 shows how the starlight intensity parameters $U_{\rm min,DL07}$ and $\overline{U}_{\rm DL07}$ are distributed over the $\sim$32 000 galaxy mask pixels (i.e., $\Sigma_{Ld}>\Sigma_{Ld,\rm min}$) where we are able to estimate the dust and starlight parameters. Half of the pixels have $\overline{U}<1$, and half of the pixels have $U_{\rm min}<1$. The $\bar{U}$ distribution for the KF62 sample (Figure 9) is similar to that for Local Group galaxies (Utomo et al. 2019).

The distributions of dust luminosity densities Σ_{Ld} and dust mass densities Σ_{Md} are displayed in Fig. 10. The Σ_{Ld} distribution peaks toward fainter Σ_{Ld}, increasing down to the lowest values of $\Sigma_{Ld}\approx10^6L_\odot\,{\rm kpc}^{-2}$ allowed by the luminosity surface density cutoff $\Sigma_{Ld,\rm min}$ defining the "galaxy mask" for each galaxy.[11] While the pixel histogram peaks at faint $\Sigma_{Ld}\approx10^6L_\odot\,{\rm kpc}^{-2}$, the infrared luminosity is dominated by the bright pixels with $\Sigma_{Ld}\approx10^8L_\odot\,{\rm kpc}^{-2}$. The distribution of dust surface densities Σ_{Md} peaks near $10^5M_\odot\,{\rm kpc}^{-2}$, which corresponds to $A_V\approx0.7$ mag, and $\sim$90% of the dust mass is contributed by pixels with $\Sigma_{Md}\gtrsim10^{4.75}M_\odot\,{\rm kpc}^{-2}$, or $A_V\gtrsim0.4$ mag. The distribution of the light-to-mass ratio Σ_{Ld}/Σ_{Md} is shown in the right panel of Fig. 10. This is of course equivalent to the distribution of $\overline{U}$. The histogram peaks at $L_{\rm d}/M_{\rm d}\approx150L_\odot/M_\odot$, corresponding to a starlight heating rate parameter $U\approx1$.

The dust light and mass surface densities that most contribute to the total dust budget are more clearly seen in Fig. 11, where we show the cumulative distributions of dust luminosity $L_{\rm d}$ and dust mass $M_{\rm d}$ plotted against Σ_{Ld} and Σ_{Md}, respectively.

The vertical dashed lines in Fig. 11 show the surface-density thresholds that provide 50% of the total: $\Sigma_{Ld}=$

[10] Using PT metallicities, Rémy-Ruyer et al. (2014) estimated this critical metallicity to be $12+\log_{10}({\rm O/H})$=8.02. Here we adjust the critical value to 8.42 to allow for the systematic offset of $\sim$0.4 between PT and PP04N2 metallicities at low O/H (see Fig. 1).

[11] Because our $\Sigma_{Ld,\rm min}$ cutoff varies from galaxy to galaxy, ranging from $10^{5.6}L_\odot\,{\rm kpc}^{-2}$ for DDO 165 to $10^{7.4}L_\odot\,{\rm kpc}^{-2}$ for NGC2146, the pixel histogram has a broad peak near $\sim10^{6.3}L_\odot\,{\rm kpc}^{-2}$.